Electronic Supporting Information

Copper(II) defect-cubane water oxidation electrocatalysts: from molecular tetramers to oxidic nanostructures

Devi Prasad Adiyeri Saseendran,[a] Jörg W. A. Fischer,[b] Lea Müller,[b] Daniel F. Abbott,[b] Victor Mougel,[b] Gunnar Jeschke,[b] Carlos A. Triana,[a] Greta R. Patzke[a]*

[a]*Department of Chemistry, Winterthurerstrasse 190, University of Zurich, CH-8057 Zurich, Switzerland.*

[b]*Department of Chemistry and Applied Biosciences, Vladimir-Prelog-Weg 1-5/10, CH-8093 Zurich, Switzerland*.

Table of Contents

Experimental section

Materials

All chemicals and solvents were obtained from commercial suppliers. All solvents were of analytical grade and used without further purification. $Cu(OAc)_2 \cdot H_2O$ (Sigma-Aldrich, 99.9% trace metal basis), $NaClO_4$ (Sigma-Aldrich), $Cu(OH)_2$ (Sigma-Aldrich, 99.0%), CuO (Sigma-Aldrich, 99.0%, nanopowder), $CuCO_3 \cdot$basic (Sigma-Aldrich, ≥95%), Triethylamine (Sigma-Aldrich, ≥99.0%), Na_2SO_4 (Sigma-Aldrich, ≥99.0%, anhydrous powder), Na_2CO_3 (Sigma-Aldrich, 99.9% trace metal basis, anhydrous powder), $NaHCO_3$ (Sigma-Aldrich, ACS reagent, ≥99.7%). Pyalk (*2-(2'-pyridyl)-2-propanoate*) ligand was purchased from 'CATALYTIC INNOVATIONS' (Adamsville, RI 02801, United States). Fluorine-doped tin oxide glass substrates (FTO, 3 mm thickness with surface resistivity ~8 Ω/sq) were purchased from Sigma Aldrich.

Characterization methods

Powder X-ray diffraction (PXRD) patterns were recorded on a STOE STADI P diffractometer (transmission mode, Ge monochromator) with Mo K_α radiation. Diffractograms were acquired in the range of 2-35 degrees with a step size of 0.05. Simulated powder XRD patterns were generated using the *Mercury 2021.1.0* software suite.[1] Attenuated total reflectance Fourier-transform infrared (ATR-FTIR) spectra were recorded on a Bruker Vertex 70 spectrometer equipped with a Platinum ATR accessory containing a diamond crystal. UV/vis spectra were recorded on a Lambda 650 S Perkin Elmer UV-Visible spectrometer in the range of 300-800 nm using a HELLMA Quartz precision cell (10 mm). Raman spectra were measured on a Renishaw System 2000 (532 nm laser with spot size ~2 μm, laser power 0.5%). Scanning electron microscopy (SEM) images were obtained using a SEM-Zeiss Supra 50, coupled with an energy-dispersive X-ray spectroscopy (EDX) detector (Genesis). The FTO electrodes were coated with 1 nm gold via sputter deposition to enhance conductivity and image clarity. XPS measurements were recorded on a Sigma II (Thermo Scientific) X-ray photoelectron spectrometer equipped with an Alpha 110 hemispherical analyzer. The instrument was operated in large-area mode using an Al K_α source at 200 W. The chamber pressure was maintained below $5 \cdot 10^{-8}$ mbar during all measurements. A pass energy of 50 eV with an energy step size of 1 eV and a 50 ms dwell time was used for collecting survey spectra. For narrow region scans, the pass energy was reduced to 25 eV, and a step size of 0.1 eV was used. High-resolution electrospray mass spectra (HR-ESI-MS) were recorded on a Bruker maXis QTOFMS

instrument (Bruker Daltonics GmbH, Bremen, Germany). The samples were dissolved in acetonitrile or water and analyzed via continuous flow injection at 3 μL/min. The mass spectrometer was calibrated between *m/z* 50 and 3000 using a Fluka electrospray calibration solution (Sigma-Aldrich, Buchs, Switzerland) at a resolution of 20'000 and a mass accuracy below 2 ppm. All pH values were measured with a calibrated pH meter (Mettler Toledo FE20). X-ray absorption near edge structure (XANES), and extended X-ray absorption fine structure (EXAFS) experiments were performed at the Swiss-Norwegian Beamline BM31, European Synchrotron Radiation Facility (ESRF), Grenoble, France. Measurements were performed at the Cu K-edge on post catalytic Cu deposit (on FTO substrates), and reference solid powder samples dispersed in cellulose of CuO, Cu_2O and $Cu(OH)_2$ (data analysis details in the following section). Low temperature X-band cw EPR spectra were recorded on an Elexsys E580 EPR spectrometer (Bruker Biospin, Rheinstetten Germany), equipped with an ESR900 helium flow cryostat (Oxford Instruments, Oxfordshire, UK) and a Super-High-Q resonator (Bruker Biospin), at ca. 9.4 GHz at 40 K. Room temperature X-band cw EPR spectra were recorded on an EMX EPR spectrometer (Bruker Biospin, Rheinstetten Germany), equipped with a Super-High-Q resonator (Bruker Biospin) operating at ca. 9.4 GHz.

Table S1. EPR measurement parameters

Experiment	Sweep width (mT)	Modulation freq. (kHz)	Modulation amp. (mT)	Attenuation (dB)	Conversion time (ms)	Time constant (ms)
Room temperature calibration	200	100	1	20	40	20
Room temperature	200	100	0.2	24	40	20
Low temperature	200	100	0.1	30	163.8	40.9

Synthesis

$[Cu_4(pyalk)_4(OAc)_4](ClO_4)(NEt_3)$ (Cu-tetramer): $Cu(OAc)_2 \cdot H_2O$ (0.19 g, 1 mmol) and $NaClO_4$ (0.18 g, 1.5 mmol) were both dissolved in acetonitrile (ACN, 25 mL). Afterward, a mixed acetonitrile (10 mL) solution of pyalk (0.068 g, 0.5 mmol) and triethylamine (70 µL, 0.5 mmol) was added dropwise to the above solution under stirring. The reaction mixture was stirred for 3 h and dried *in vacuo* using a rotary evaporator. Afterward, the Cu-tetramer complex was extracted with dichloromethane (DCM, 20 mL), followed by the addition of excess Na_2SO_4. Finally, the DCM extract was filtered through celite and reduced to half volume using rotary evaporation. A dark blue slurry was obtained by slow evaporation of this DCM solution at room temperature overnight, which was further dried under a high vacuum to obtain a blue solid (0.32 g, yield: 43% on Cu). Intense blue-coloured single crystals of the Cu-tetramer were obtained via vapour diffusion of n-pentane into the DCM solution of the complex over 2 weeks. HRMS (ESI) *m/z*: $[Cu_3L_3(OAc)_2]^+$ calcd. for $C_{28}H_{36}N_3O_7Cu_3$: 715.0435; found, 715.0431.

$[Cu_2(pyalk)_2(OAc)_2(H_2O)_2]$ (Cu-dimer): The Cu-dimer complex was obtained by dissolution of the Cu-tetramer complex in Milli-Q water. Specifically, Cu-tetramer (0.3 g, 0.2 mmol) complex was dissolved in Milli-Q H_2O (10 mL) and stirred for 1 h. The resulting solution was filtered and transferred to a crystallizing dish. Diamond-shaped, blue crystals were obtained over 4 weeks via slow evaporation of this aqueous solution at room temperature. The crystals were washed with n-hexane followed by ice-cold ethanol and filtered (0.056 g, yield: 95%). HRMS (ESI) *m/z*: $[Cu_2L_2(H_2O)]^+$ calcd. for $C_{18}H_{23}N_2O_4Cu_2$: 457.0244; found, 457.0245. Elemental Anal. calcd. for molecular formula $C_{20}H_{34}Cu_2N_2O_{10}$: C 40.74%, H 5.81%, N 4.75%; found: C 40.64%; H 5.60%; N 4.20%.

UV/vis: λ_{max} 655 nm (ε = 85 M^{-1} cm^{-1}, carbonate-bicarbonate buffer pH 10.5)

CCDC 2215584 (Cu-dimer) and CCDC 2243591 (Cu-tetramer) contain the supplementary crystallographic data for this paper. These data can be obtained free of charge from the Cambridge Crystallographic Data Centre via www.ccdc.cam.ac.uk/data_request/cif.

Single crystal X-ray diffraction

Suitable single crystals were selected on a *Leica* polarizing microscope, mounted on a glass fiber loop with Infineum oil and measured on an XtaLAB Synergy, Dualflex, Pilatus 200K diffractometer (Rigaku Oxford) equipped with a Photonjet (Mo and Cu) X-ray source (Mo K_α, λ = 0.71073 Å; Cu K_α, λ =1.54184 Å) and a mirror monochromator (cooled N_2 stream at 160 K). The data processing and absorption correction (Gaussian or Multi-scan) were carried out using the program CrysAlisPro 1.179.39.46 (Rigaku Oxford Diffraction, 2018). Structure solutions and refinements were performed using the Olex2 1.5 software package.[2] The initial structures were obtained with the intrinsic phasing method using SHELXT (2018/2)[3] and refined with full-matrix least-square methods on F2 using SHELXL (2018/3).[4] The H atoms of all hydroxyl groups, all aqua ligands, and a part of solvent water were acquired according to the difference Fourier map and their positions were refined freely along with individual isotropic displacement parameters. The solvent water O atoms without reliable difference Fourier maps positioning their H atoms were only anisotropically refined without adding H. All such H numbers were still included in UNIT to obtain the correct formulas. The remaining H atoms were placed in geometrically idealized positions and were constrained to ride on their parent atoms with C-H = 0.95 Å (aryl) or 0.98 Å (methyl) and U_{iso}(H) = 1.2 Ueq(C) (aryl) or 1.5 U_{eq}(C) (methyl).

XAS data treatment

XAS data were acquired from the Swiss-Norwegian Beamline BM31 at the European Synchrotron Radiation Facility (ESRF), Grenoble, France. Measurements were performed at room temperature using a three-ionization chamber configuration in transmission mode for CuO, Cu_2O and $Cu(OH)_2$ (reference samples). The XANES-EXAFS spectra of the Cu deposit on FTO substrates were measured in fluorescence mode. For energy calibration, the spectrum of a metal Cu foil was measured simultaneously at the second ionization chamber. The storage ring was run in top-up mode with a current of 40 mA. The X-ray beam was collimated using a Si coated mirror and energy was scanned using a double crystal Si[111] monochromator. The measured EXAFS spectra $k^3\chi(k)$ were extracted by standard data reduction, absorption edge energy calibration and background subtraction as implemented in ATHENA.[5] The spectra were reduced into the range $\Delta k \approx 3\text{-}12$ Å^{-1} and Fourier transformed to FT$|k^3\chi(k)|$ into the real-space

interval of ΔR≈0-6 Å. To calculate main values for interatomic distances, coordination numbers, and Debye-Waller factors σ^2 nonlinear least-squares fitting of the experimental FT|$k^3\chi(k)$| spectra was carried out by ARTEMIS[5] using atomic clusters of CuO (ICSD code 16025), generated by ATOMS[5] as implemented in IFEFFIT.[5] The amplitudes and phases shift for single and multiple scattering paths were calculated using FEFF6.[6]

Electrochemistry and oxygen evolution measurements

Electrochemical measurements were performed using a MetrOhm AUTOLAB Potentiostat. During cyclic voltammetry (CV) or controlled potential electrolysis, an Ag/AgCl (3 M KCl) reference electrode and a Pt auxiliary electrode were used. CV experiments were performed with glassy carbon working electrodes with an active area of 0.070 cm^2, whereas large surface area (1 x 1 cm) FTO electrodes were used for bulk electrolysis experiments. All potentials have been referenced to Ag/AgCl (3 M KCl) electrode. Oxygen evolution measurements were performed in an air-tight electrochemical H-cell containing 0.5 mM Cu-dimer complex in 0.08 M carbonate-bicarbonate buffer (pH 10.5), FTO working electrode, an Ag/AgCl (3 M KCl) reference electrode, Pt counter electrode, and a Clark type electrode for oxygen detection. The air saturated oxygen concentration in water was calculated prior to catalytic measurements and the sensor was calibrated to obtain baseline readings. Zero oxygen concentration readings were recorded using an anoxic solution made of sodium ascorbate and sodium hydroxide. A bias of 1.65 V vs. NHE was applied to the electrochemical cell to initiate water oxidation catalysis over 7 h. The 0.5 mM solution of Cu-dimer complex buffer solution was thoroughly purged with argon before commencing bulk electrolysis. The theoretical amount of oxygen was calculated by dividing the recorded charge passed by 4 F (F = Faraday constant = 96845 C mol^{-1}), where the Faradaic Efficiency (FE) was calculated as follows:[7–10]

$$\text{FE (\%)} \quad \frac{n_{\text{meas O2}}}{n_{\text{calcd O2}}} \times 100$$

Table S2. Crystallographic data and structure refinement parameters for the Cu-tetramer complex.

Identification code	$Cu_4(pyalk)_4(OAc)_4$_tetramer
Empirical formula	$C_{104}H_{180}Cl_4Cu_8N_{12}O_{45}$
Formula weight	2968.71
Temperature/K	160.00(10)
Crystal system	monoclinic
Space group	$P2_1/n$
a/Å	9.15690(10)
b/Å	31.5203(3)
c/Å	11.78070(10)
α/°	90
β/°	97.8590(10)
γ/°	90
Volume/Å^3	3368.31(6)
Z	1
ρ_{calc}g/cm^3	1.464
μ/mm^{-1}	2.789
F(000)	1548.0
Crystal size/mm^3	0.091 × 0.063 × 0.063
Radiation	Cu K_α (λ = 1.54184)
2Θ range for data collection/°	5.608 to 147.138
Index ranges	-10 ≤ h ≤ 11, -38 ≤ k ≤ 39, -14 ≤ l ≤ 14
Reflections collected	43173
Independent reflections	6646 [R_{int} = 0.0373, R_{sigma} = 0.0231]
Data/restraints/parameters	6646/0/412
Goodness-of-fit on F^2	1.049
Final R indexes [I>=2σ (I)]	R_1 = 0.0360, wR_2 = 0.1072
Final R indexes [all data]	R_1 = 0.0424, wR_2 = 0.1113
Largest diff. peak/hole / e Å^{-3}	0.89/-0.47

$R_1 = \Sigma||F_o| - |F_c||/\Sigma|F_o|$, $wR_2 = [\Sigma(|F_o|^2 - |F_c|^2)^2/\Sigma(F_o^2)]^{1/2}$

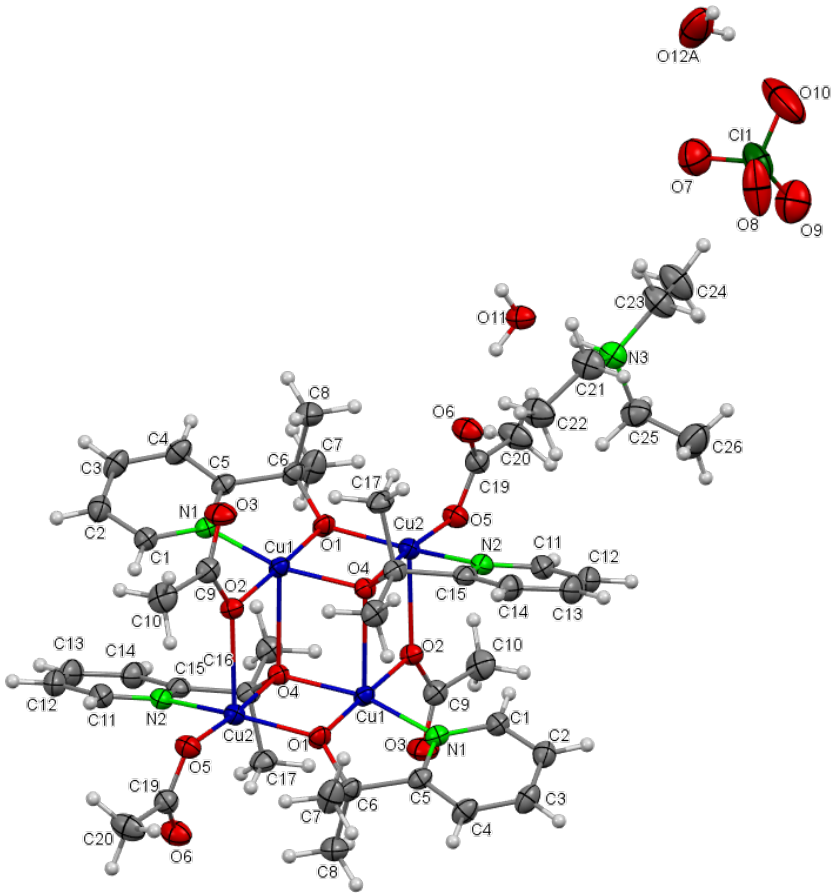

Figure S1. *ORTEP* representation of the **Cu-tetramer** complex (50% ellipsoidal probability).

Table S3. Selected bond lengths of the **Cu-tetramer** complex.

Bond	**d (Å)**
Cu1-O4	1.9814 (16)
Cu1-O1	1.9086 (16)
Cu1-O2	1.9446 (16)
Cu1-N1	1.998 (2)
Cu2-O4	1.9768 (16)
Cu2-O1	1.9462 (16)
Cu2-O2	2.3840 (16)
Cu2-O5	1.9361 (17)
Cu2-N2	2.000 (2)

Table S4. Crystallographic data and structure refinement parameters for the Cu-dimer complex.

Identification code	$Cu_2(pyalk)_2(OAc)_2$
Empirical formula	$C_{20}H_{34}Cu_2N_2O_{10}$
Formula weight	589.57
Temperature/K	160.00(10)
Crystal system	triclinic
Space group	*P-1*
a/Å	8.02330(10)
b/Å	8.8028(2)
c/Å	9.65090(10)
α/°	71.0760(10)
β/°	86.2810(10)
γ/°	77.2790(10)
Volume/Å^3	628.935(18)
Z	1
ρ_{calc} g/cm^3	1.557
μ/mm^{-1}	1.745
F(000)	306.0
Crystal size/mm^3	0.256 × 0.181 × 0.137
Radiation	Mo K_α (λ = 0.71073)
2Θ range for data collection/°	4.462 to 75.842
Index ranges	-13 ≤ h ≤ 13, -14 ≤ k ≤ 15, -16 ≤ l ≤ 16
Reflections collected	58956
Independent reflections	6442 [R_{int} = 0.0360, R_{sigma} = 0.0208]
Data/restraints/parameters	6442/0/173
Goodness-of-fit on F^2	1.062
Final R indexes [I>=2σ (I)]	R_1 = 0.0247, wR_2 = 0.0642
Final R indexes [all data]	R_1 = 0.0310, wR_2 = 0.0662
Largest diff. peak/hole / e Å^{-3}	0.51/-0.61

$R_1 = \Sigma||F_o| - |F_c||/\Sigma|F_o|$, $wR_2 = [\Sigma(|F_o|^2 - |F_c|^2)^2/\Sigma(F_o^2)]^{1/2}$

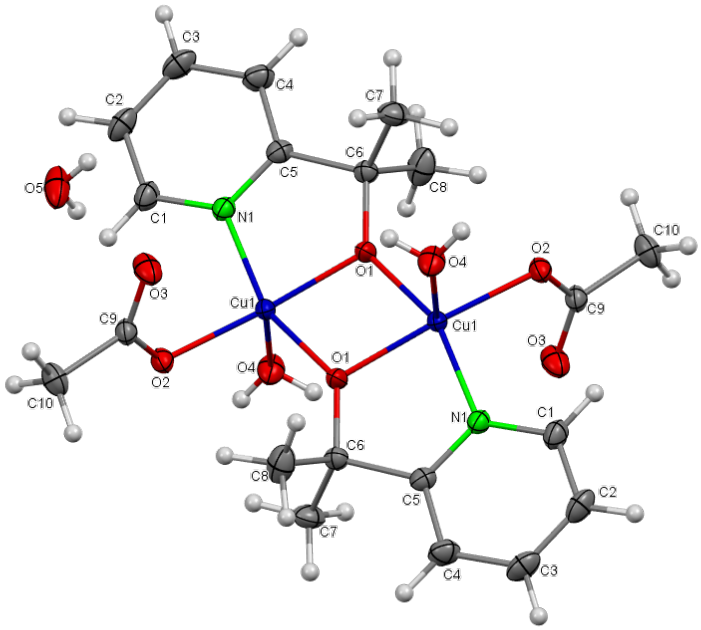

Figure S2. *ORTEP* representation of the **Cu-dimer complex** (50% ellipsoidal probability)**.**

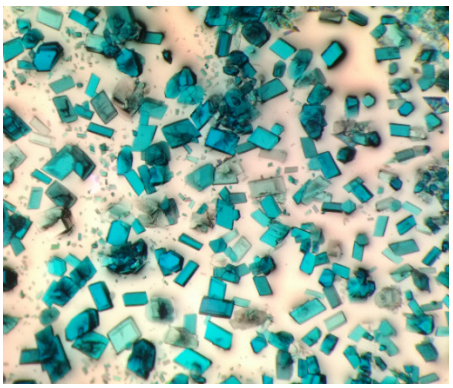

Figure S3. Single crystals of the **Cu-dimer complex** obtained in bulk (after the dissolution of the Cu-tetramer in H_2O)

Table S5. Selected bond lengths of the **Cu-dimer** complex

Bond	**d (Å)**
Cu1-O1	1.9187 (6)
Cu1-O1[1]	1.9435 (6)
Cu1-O2	1.9583 (6)
Cu1-O4	2.3178 (7)
Cu1-N1	1.9825 (7)

[1]1-X, 1-Y, 2-Z

UV-Visible spectroscopy

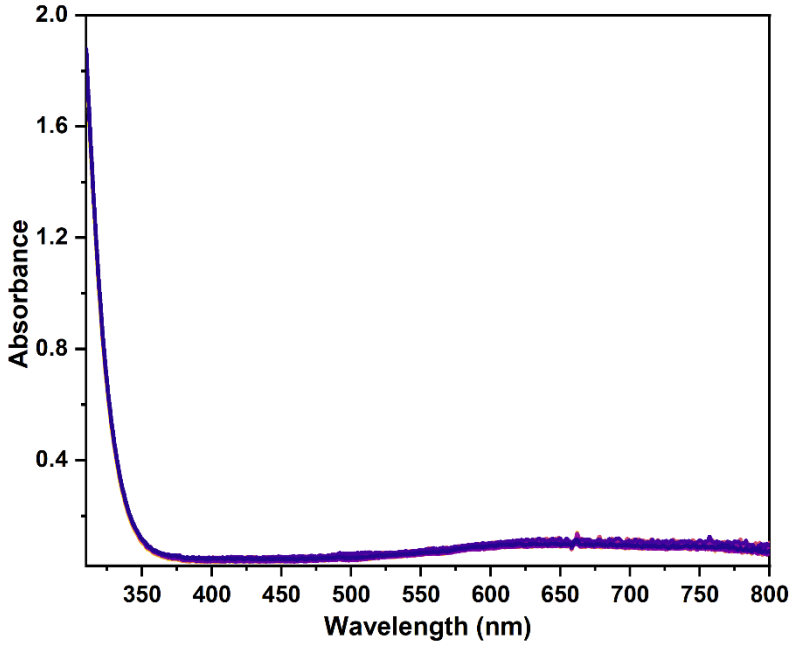

Figure S4. Time-dependent UV-vis spectra of 0.5 mM **Cu-dimer** complex in 0.08 M carbonate-bicarbonate buffer (pH 10.5) over 24 h.

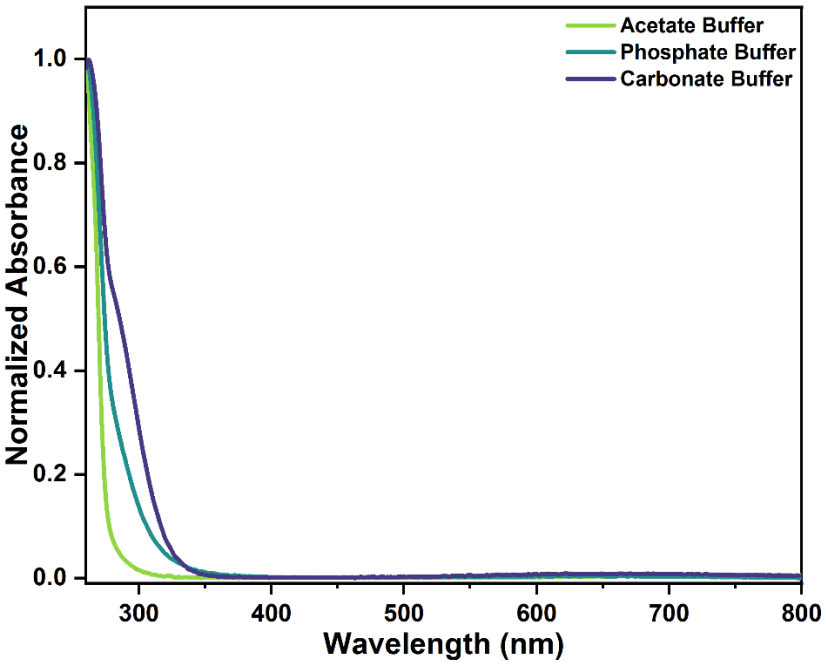

Figure S5. UV-vis spectra of 0.05 mM **Cu-dimer** complex in acetate, phosphate and carbonate buffer. The data has been normalized into the 0-1 interval because a comparison of the absorption bands in the UV region cannot be done without normalization since the absorption values differ in each case.

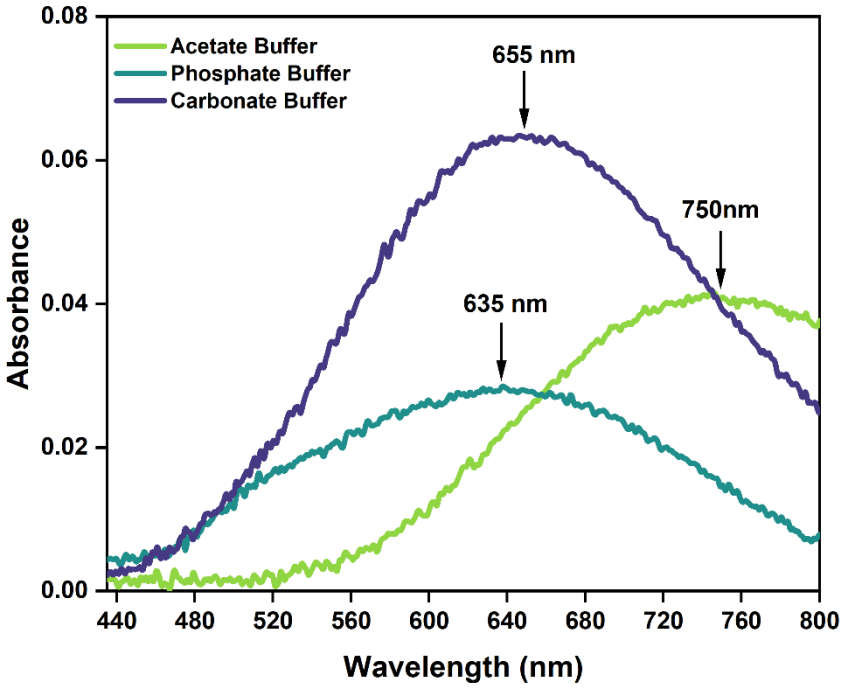

Figure S6. UV-vis spectra of 0.5 mM **Cu-dimer** complex in acetate, phosphate and carbonate buffer, depicting the shifts in *d-d* bands.

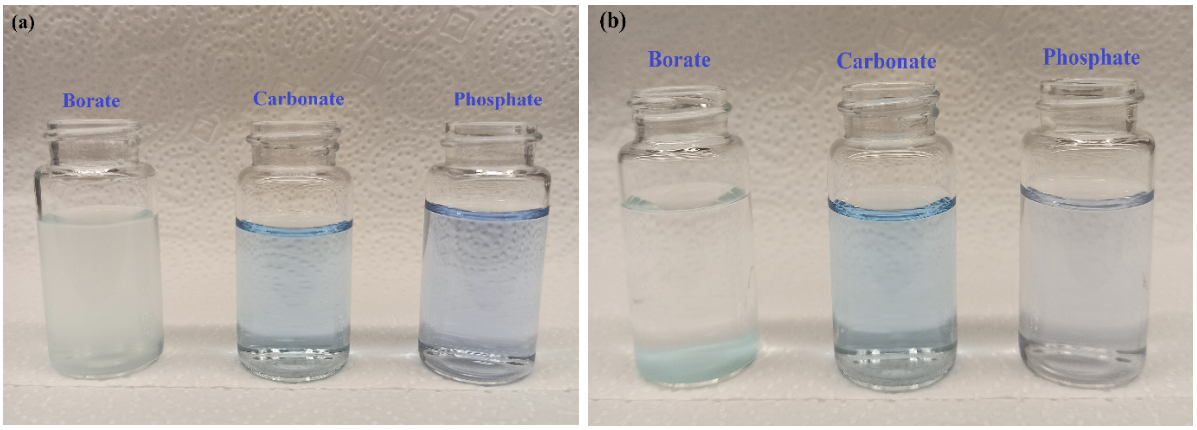

Figure S7. **Cu-dimer** complex dissolved in borate, carbonate, and phosphate buffer (a) immediately after dissolution, (b) after 20 minutes.

Electron paramagnetic resonance (EPR) spectroscopy

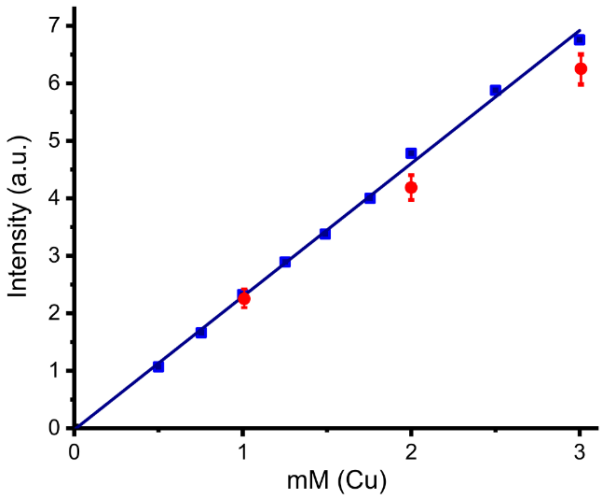

Figure S8. Quantitative analysis of EPR active Cu species in different solutions of monomeric Cu (red) and data for $CuSO_4$ reference solutions (blue).

Cu-dimer was dissolved to concentrations of 1, 2, and 3 mM in buffer and continuous wave (cw) EPR spectra were measured to determine monomer concentrations. The double integral intensity of such spectra is proportional to the total number of spins in the sample. Species with an even number of strongly antiferromagnetically coupled Cu(II) ions do not contribute to the EPR signal. Therefore, the concentration of monomeric Cu(II) species can be quantified by comparing the double integral of the EPR spectrum of an unknown to double integrals of spectra of reference solutions with a known concentration. Here, an aqueous solution of $CuSO_4$ was used for reference. Up to a concentration of 1 mM Cu ions or 0.5 mM Cu-dimer concentration, respectively, all copper seems to be present in a monomeric form. Increasing the concentration leads to a small fraction of EPR silent Cu species, which are presumably Cu-dimers.

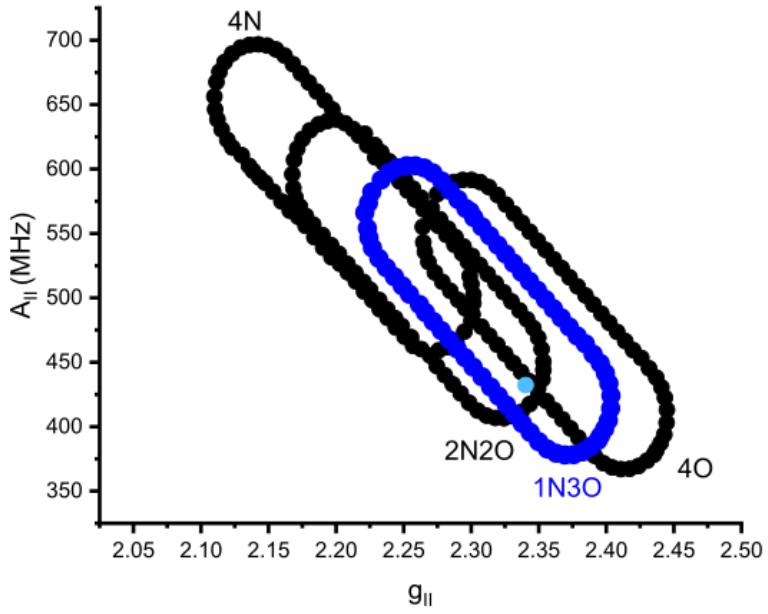

Figure S9. $A_{||}$ versus $g_{||}$ for various copper coordination spheres. Data adapted from Peisach *et al.*[11] The light blue point corresponds to spin Hamiltonian parameters of the monomer in carbonate buffer at 10.5 pH.

The Bloomberg-Peisach plot[11] of the monomeric Cu complex freeze-quenched without cryoprotectant in carbonate buffer at pH 10.5 is depicted in Figure S7. The correlation of $g_{||}$ and $A_{||}$ indicates a coordination sphere of one nitrogen and three oxygen atoms. The cw EPR spectrum at 40 K (Figure S8) clearly exhibits the partially resolved superhyperfine couplings from one nitrogen ligand.

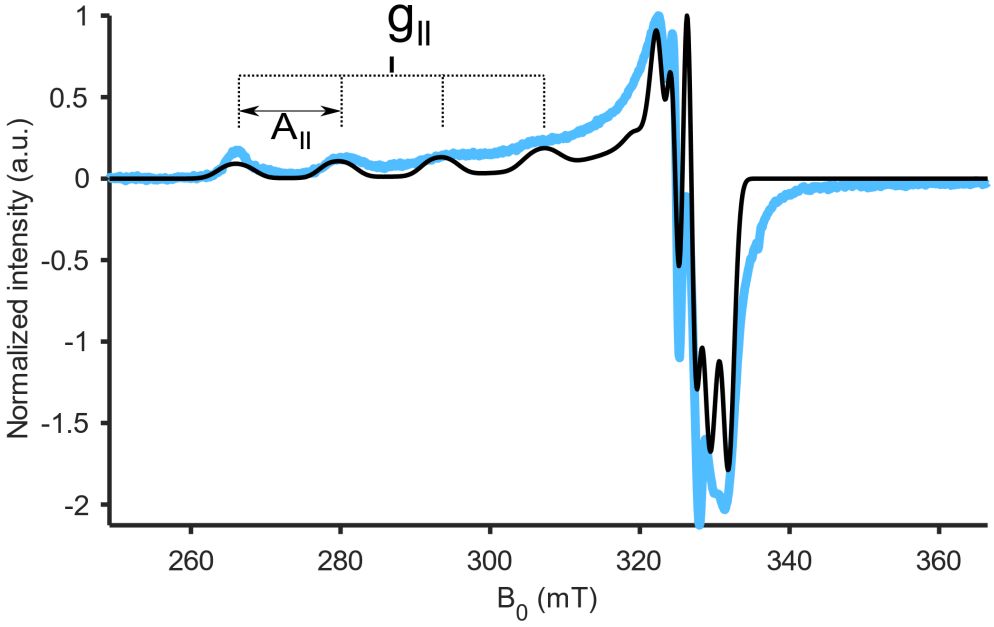

Figure S10. X-band cw EPR spectrum of the freeze-quenched Cu complex at 40 (light blue: experimental spectrum; black: simulations). The respective parameters can be found in Table S6. The $g_{||}$ and the $A_{||}$ values used in the Bloomberg-Peisach analysis are indicated.

Table S6. Simulation parameters for the Cu-monomer complex at 40 K. All simulations were performed with the MATLAB toolbox EasySpin.[12] The anisotropic contribution to the ^{14}N hyperfine tensor is not expected to be resolved and was therefore neglected.

	Cu Monomer
g	$g_{\perp}$: 2.057 $g_{\parallel}$: 2.34
gStrain	0.011 0.025
Cu (MHz)	$A_{\perp}$: 27.5 $A_{\parallel}$: 438
N (MHz)	A_{iso}: 55

HR-ESI mass spectrometry

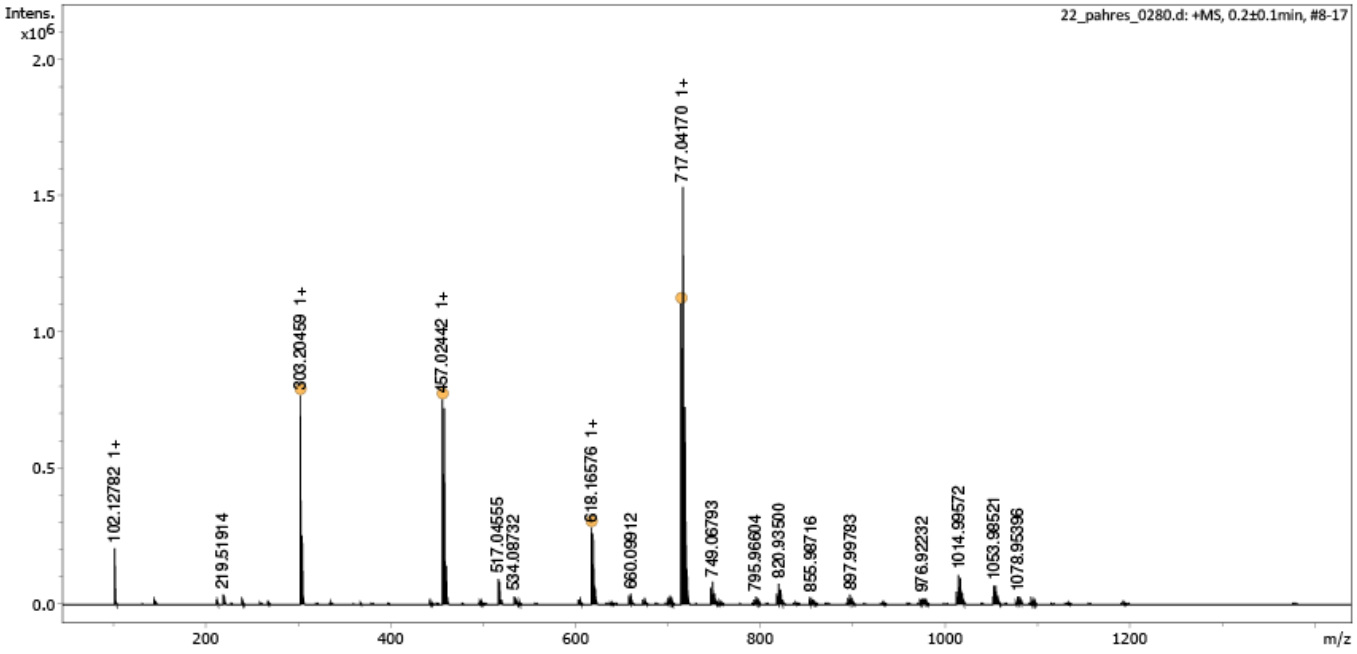

Figure S11. ESI-HRMS spectrum of the **Cu-tetramer** in acetonitrile

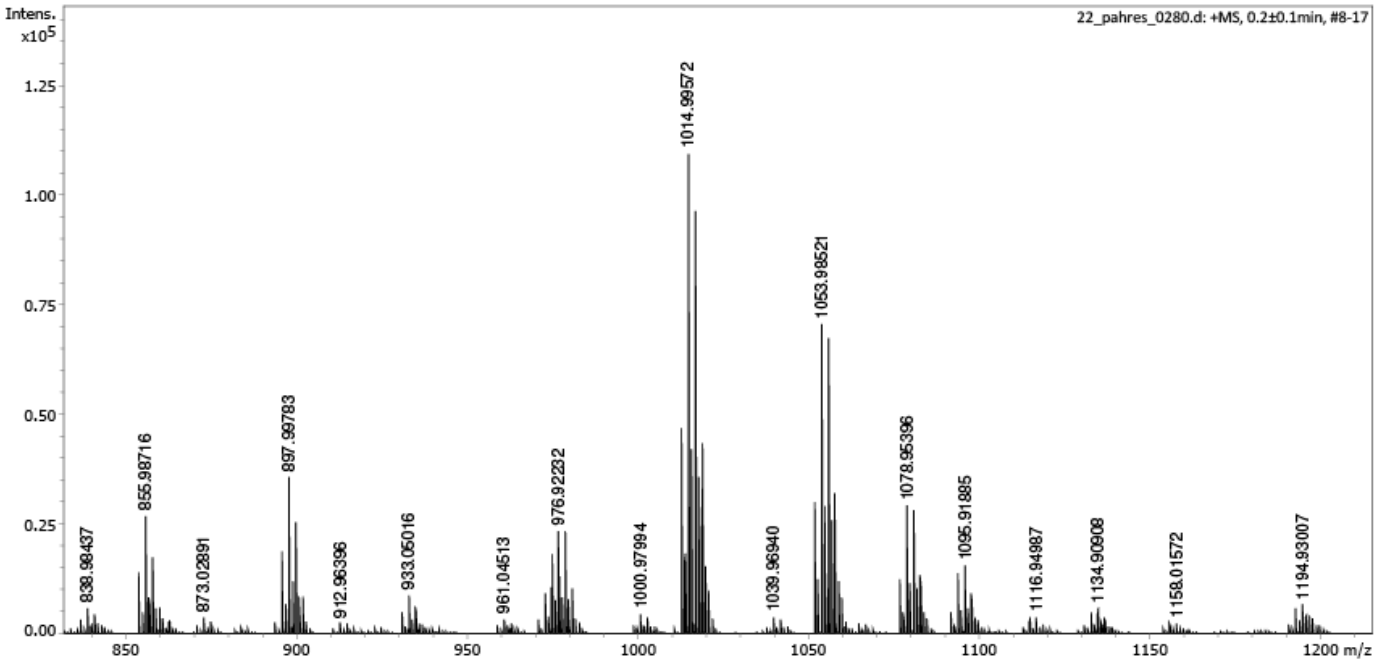

Figure S12. ESI-HRMS spectrum of the **Cu-tetramer** in acetonitrile (focusing the peak at m/z = 1053.98)

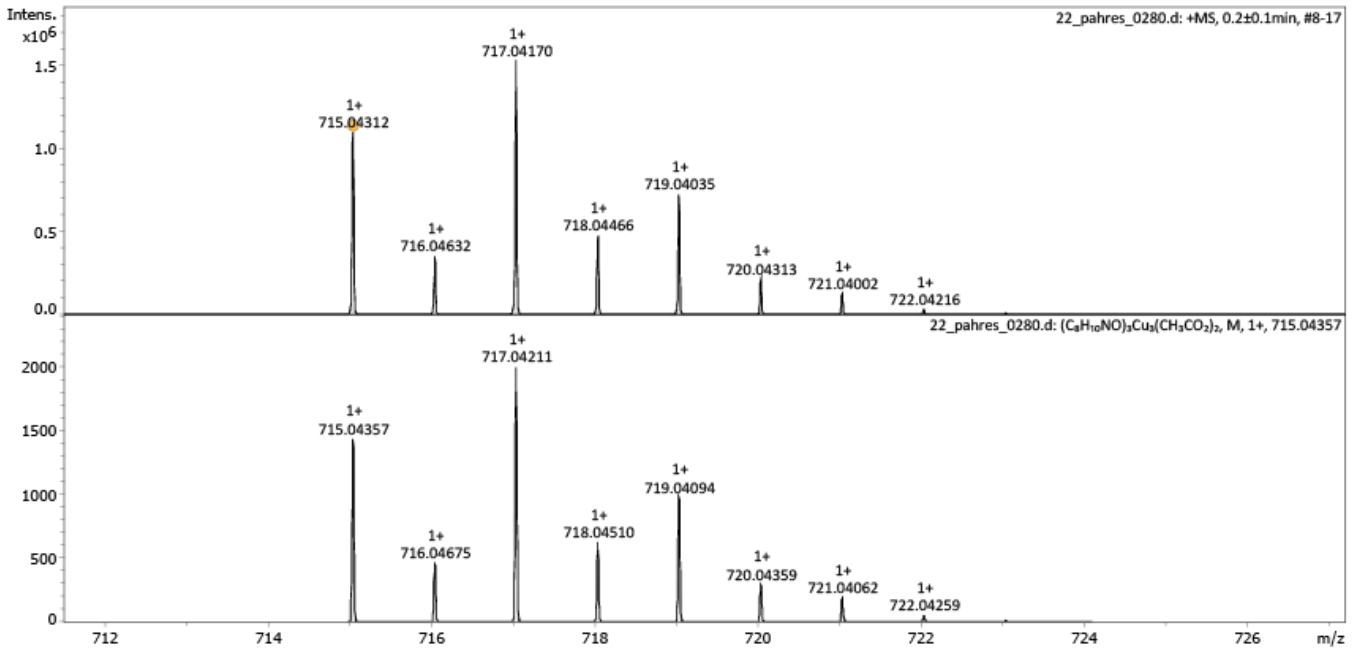

Figure S13. Calculated and observed isotopic patterns in the ESI-HRMS spectrum of the **Cu-tetramer** in acetonitrile.

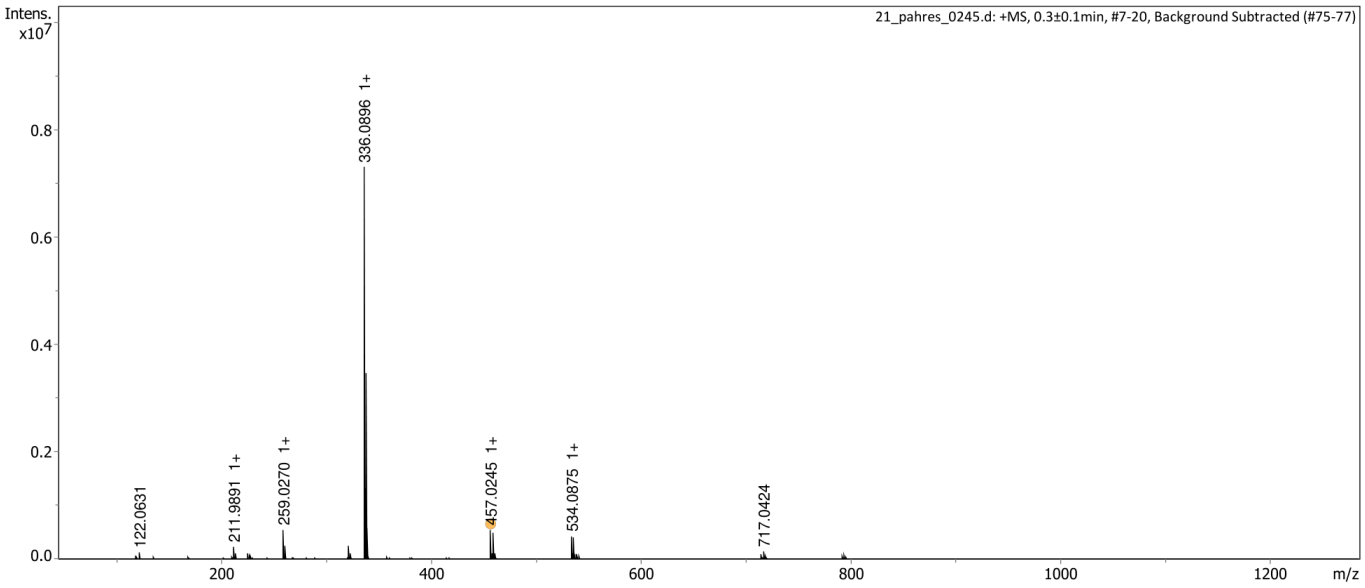

Figure S14. ESI-HRMS spectrum of the **Cu-tetramer** in water.

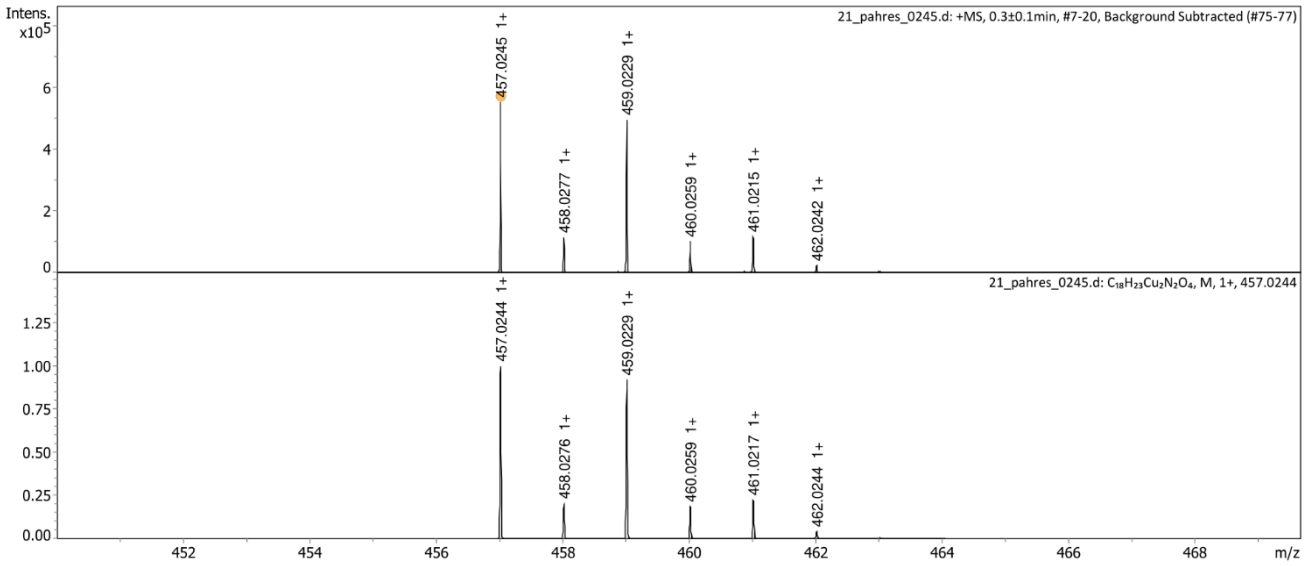

Figure S15. Calculated and observed isotopic patterns in the ESI-HRMS spectrum of the **Cu-tetramer** in water.

Powder X-ray diffraction

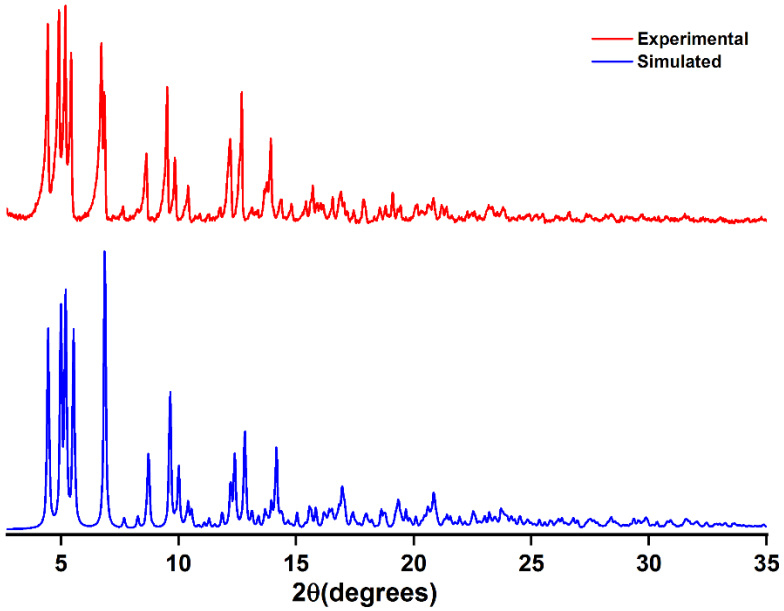

Figure S16. Experimental and simulated powder X-ray diffraction patterns of the **Cu-dimer** complex.

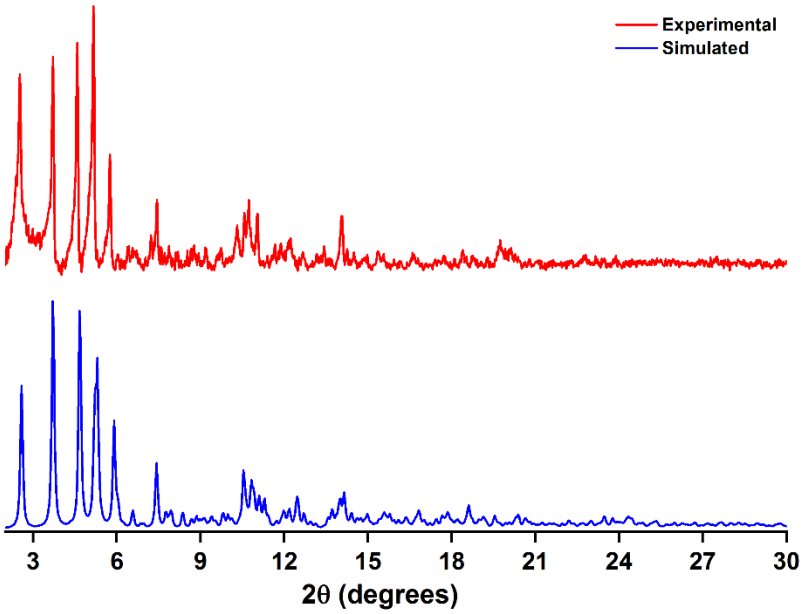

Figure S17. Experimental and simulated powder X-ray diffraction patterns of the **Cu-tetramer** complex.

Raman spectroscopy

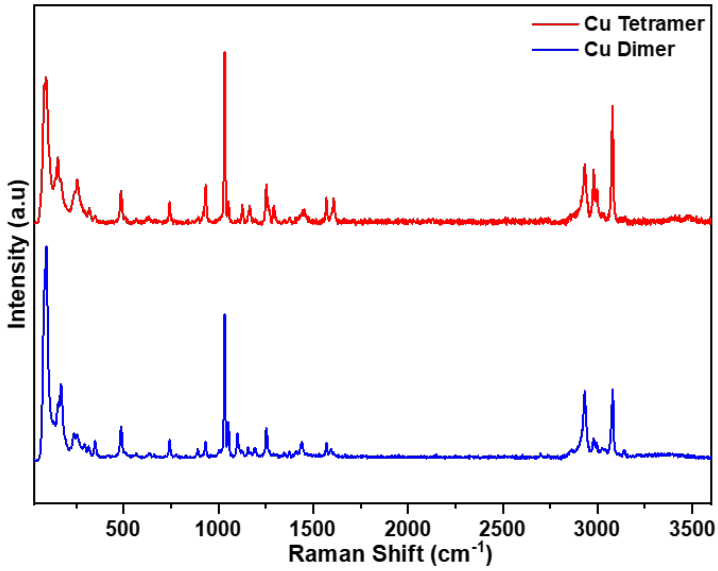

Figure S18. Raman spectra of the **Cu-tetramer** and **Cu-dimer** complexes.

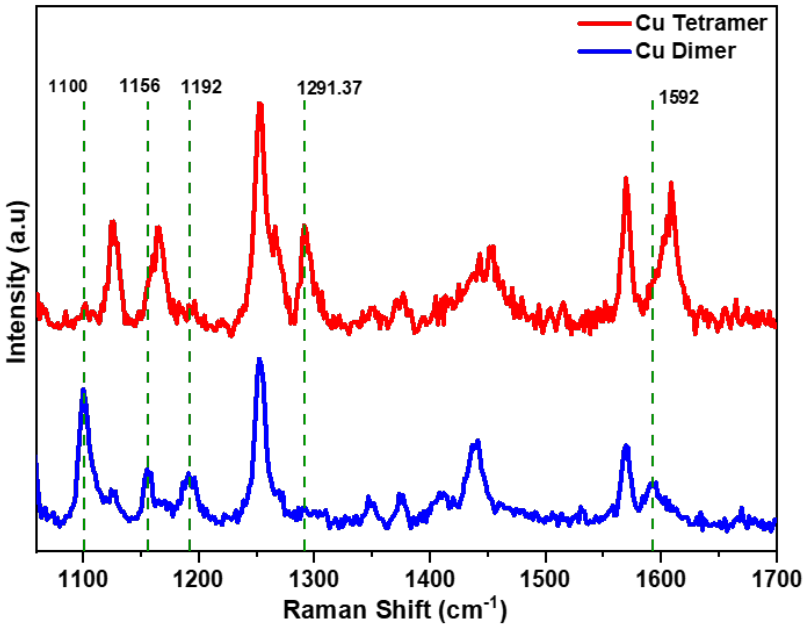

Figure S19. Raman spectra of the **Cu-tetramer** and **Cu-dimer** complexes in the 1000-1700 cm^{-1} region.

FT-IR spectroscopy

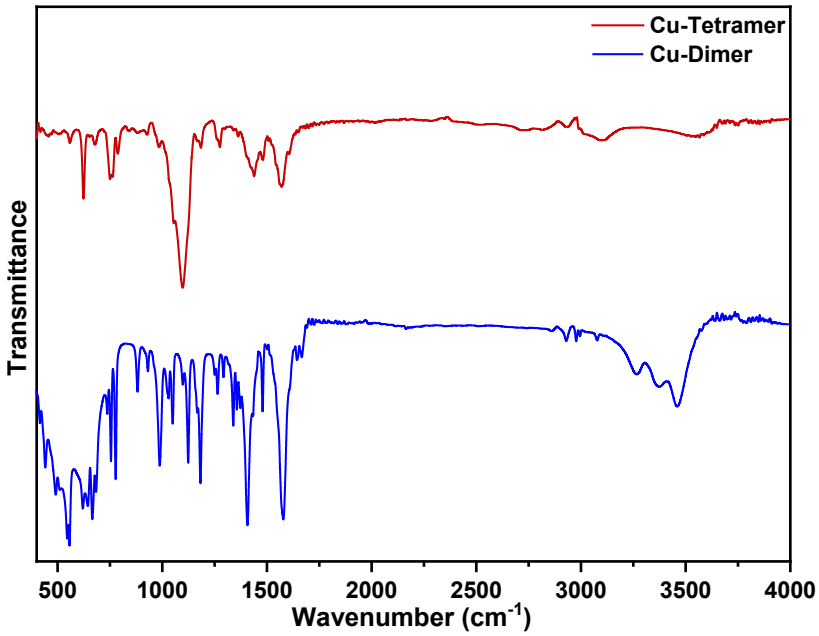

Figure S20. FT-IR spectra of the **Cu-tetramer** and **Cu-dimer** complexes.

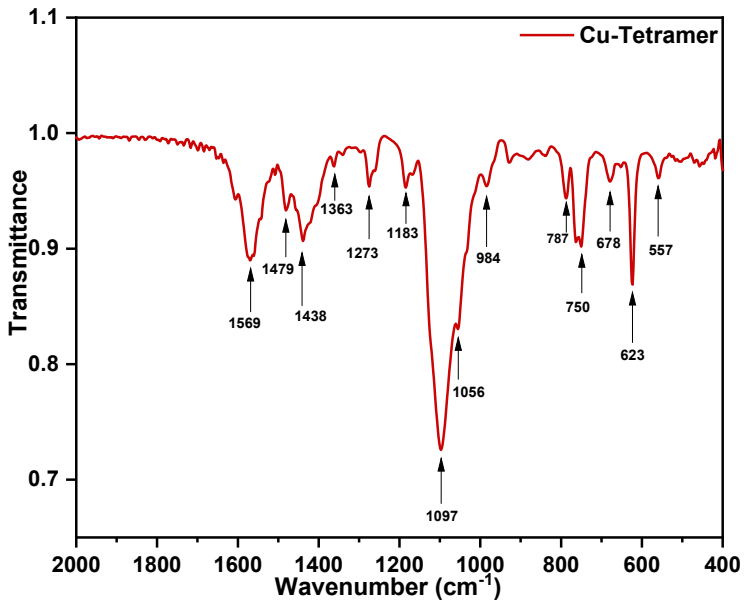

Figure S21. FT-IR spectra of the **Cu-tetramer** complex in the fingerprint region.

1183 cm^{-1}, 1097 cm^{-1}: single C-O stretching vibration of the *pyalk* ligand (Cu bound);
1438 cm^{-1}, and **1363 cm^{-1}**: stretching vibrations of the pyridyl rings;
1479 cm^{-1}: C=N vibrations of the pyridyl rings;
1569 cm^{-1}: asymmetrical vibrations of COO^-; **1363 cm^{-1}** : symmetric vibrations of COO^- ;
984 cm^{-1}, 623 cm^{-1} : ν4(F2) of the uncoordinated T_d ClO_4^- (shifted due to H-bonding interactions);

678 cm^{-1}, **787 cm^{-1}**, and **750 cm^{-1}**: C-H out-of-plane vibrations of the pyridyl rings; C-H in-plane vibrations of the pyridyl rings
557 cm^{-1}: out of plane bending of pyridyl rings

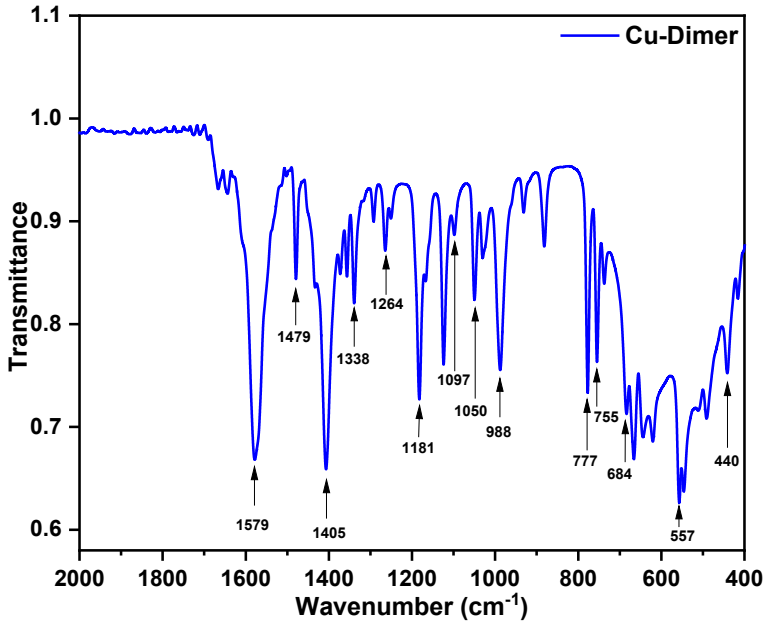

Figure S22. FT-IR spectra of the **Cu-dimer** complex in the fingerprint region.

1050 cm^{-1}, 1097 cm^{-1}: single C-O stretching vibration of the *pyalk* ligand (Cu bound);
1405 cm^{-1}, and **1338 cm^{-1}**: stretching vibrations of the pyridyl rings;
1479 cm^{-1}: C=N vibrations of the pyridyl rings;
1579 cm^{-1}: asymmetrical vibrations of COO^-;
684 cm^{-1}, **777 cm^{-1}**, and **755 cm^{-1}**: C-H out-of-plane vibrations of the pyridyl rings; C-H in-plane vibrations of the pyridyl rings
440 cm^{-1} and **557 cm^{-1}**: out-of-plane bending of pyridyl rings

Electrochemical characterization

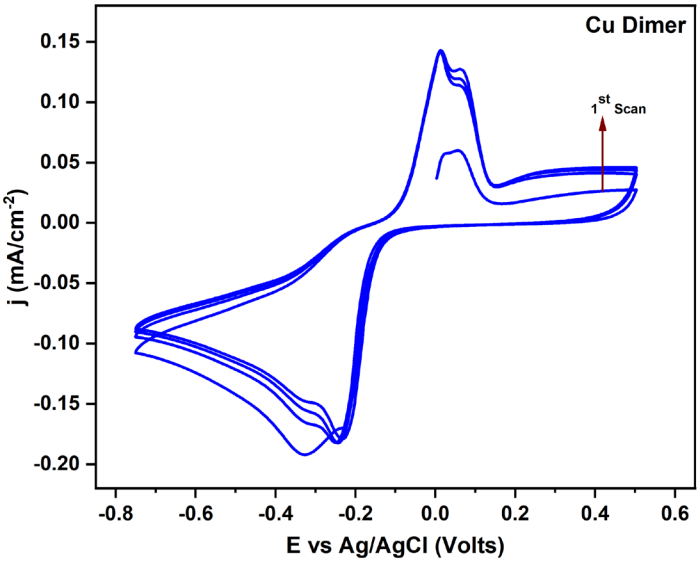

Figure S23. CV of 0.5 mM Cu-complex (scan rate 30 mV/s) in 0.08 M carbonate-bicarbonate buffer (pH =10.5), showing the redox events.

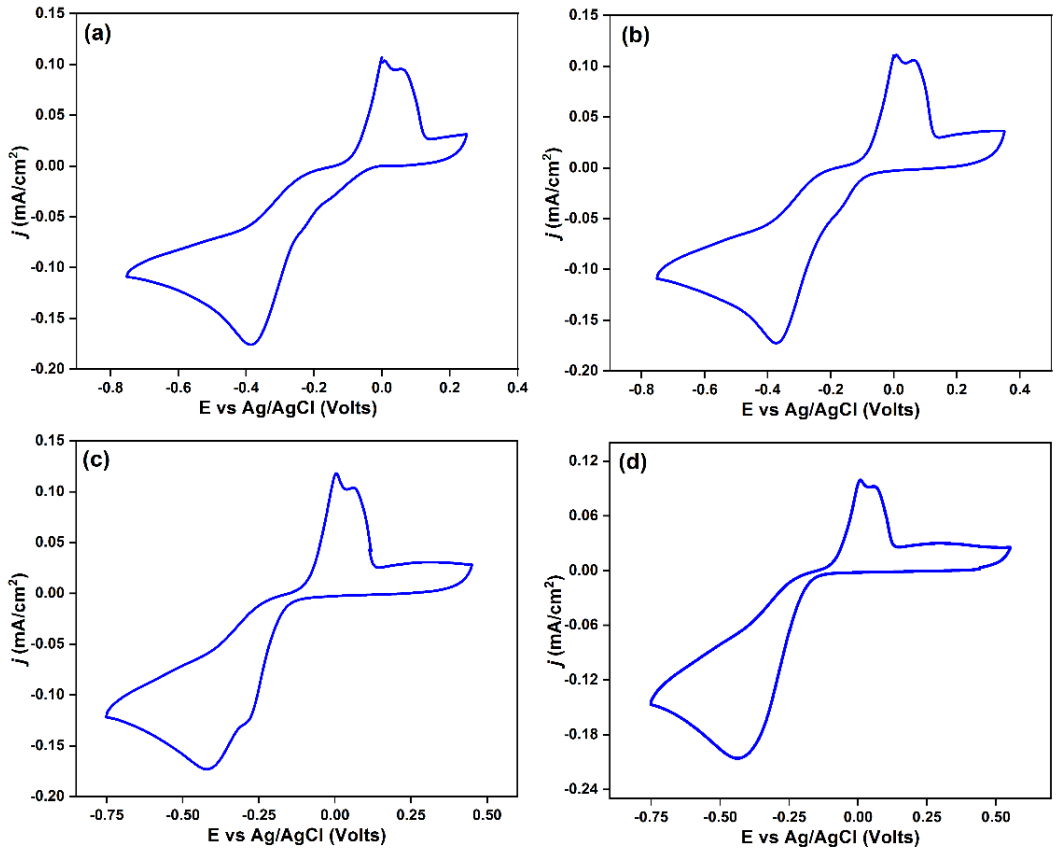

Figure S24. CVs of 0.5 mM Cu-complex (scan rate 50 mV/s) in 0.08 M carbonate-bicarbonate buffer (pH 10.5), scanned from -0.75 V to anodic potential ranges of (a) +0.25 V, (b) +0.35 V, (c) +0.45 V, (d) +0.55 V.

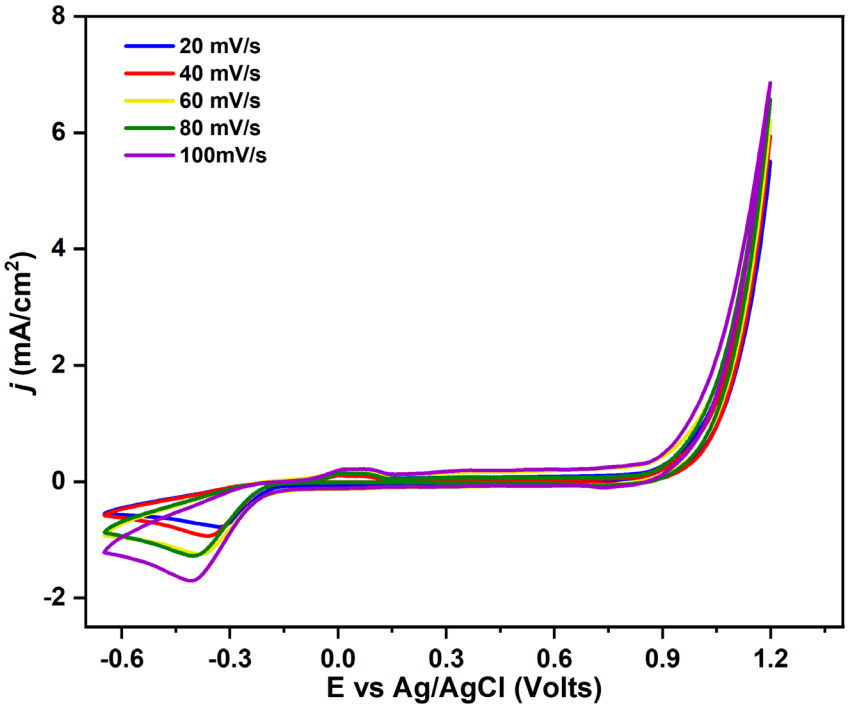

Figure S25. CVs of 0.5 mM Cu-complex in 0.08 M carbonate-bicarbonate buffer (pH 10.5) at different scan rates.

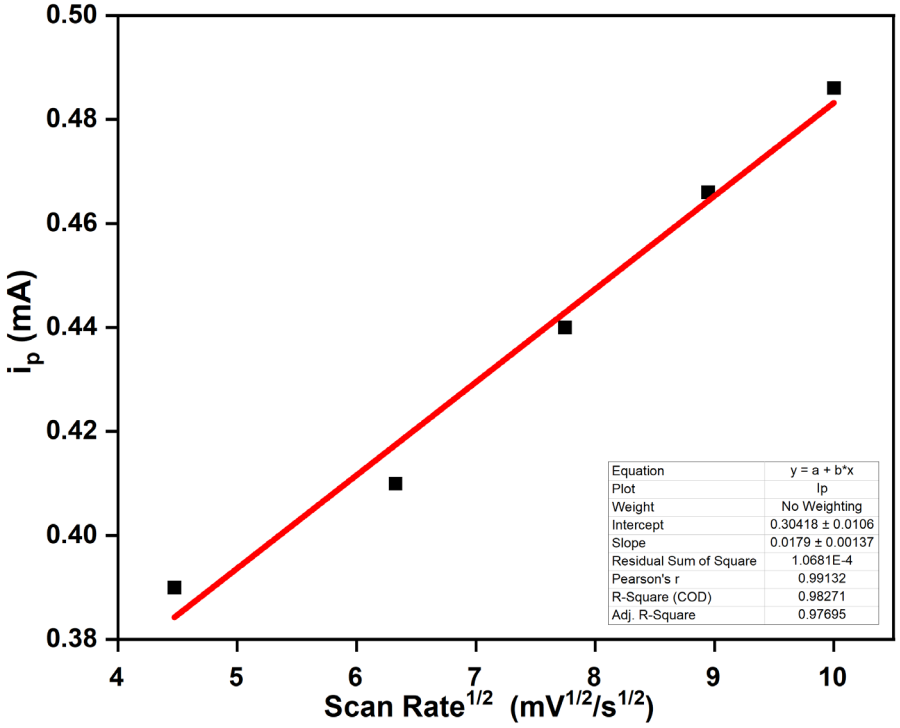

Figure S26. Variation of peak current with square root of scan rate (as per Randles-Sevcik Equation).

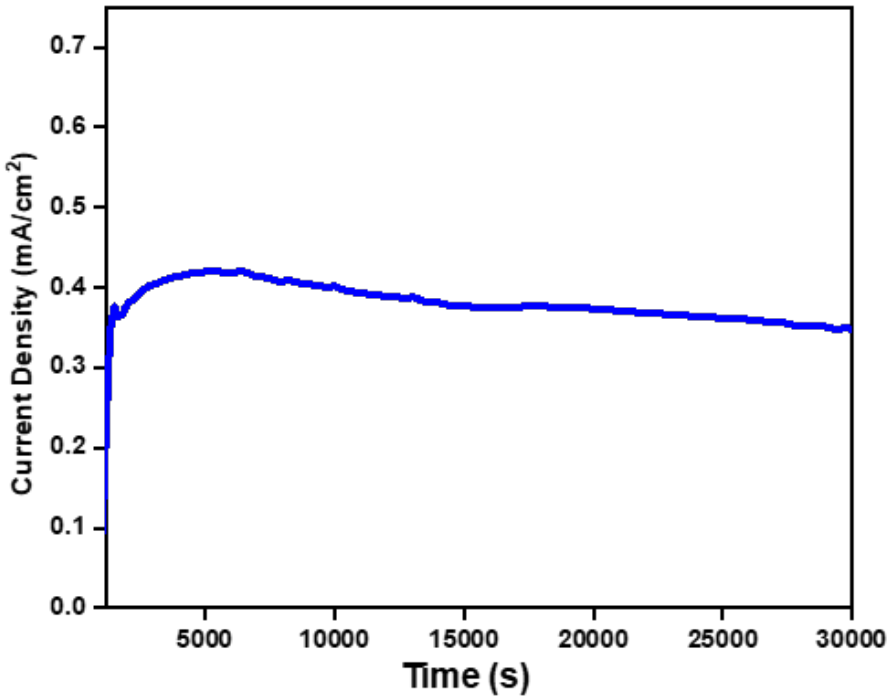

Figure S27. Controlled potential electrolysis profile of 0.5 mM Cu-dimer, at an applied potential of 0.82 V (*vs* Ag/AgCl) for 7 h.

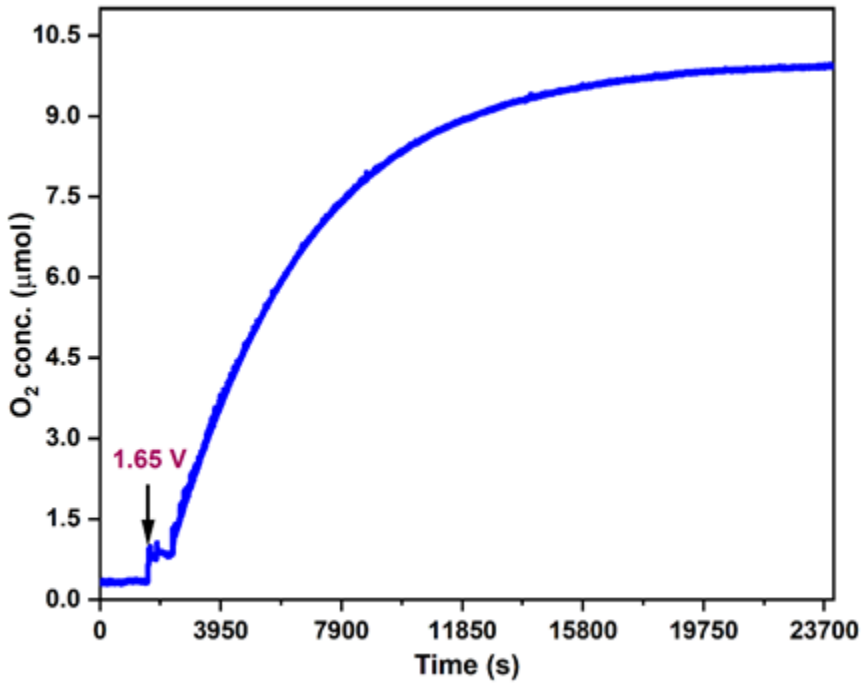

Figure S28. Oxygen evolution measured with a Clark electrode, during CPE at 0.82 V (1.65 V vs NHE), for 7 h.

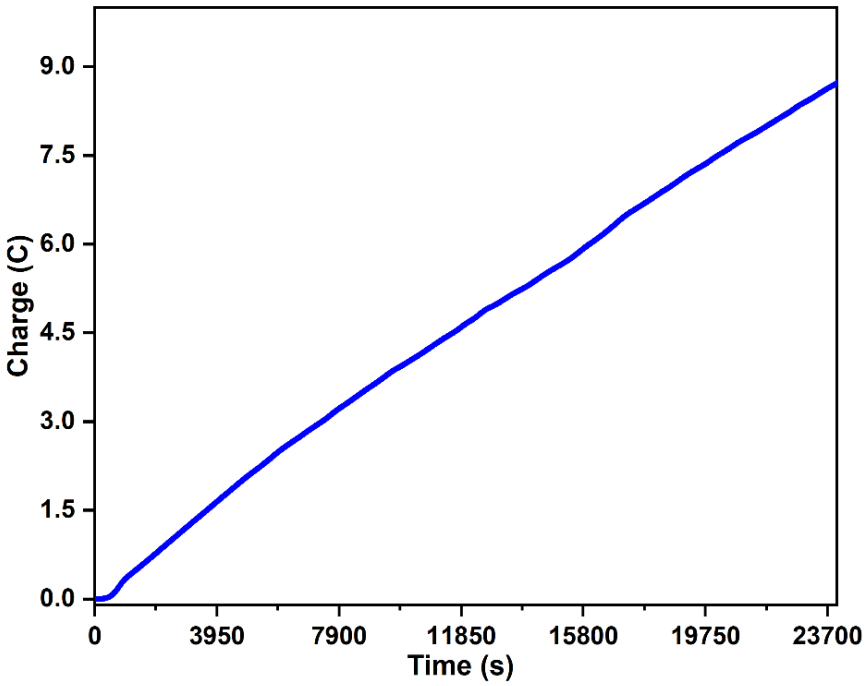

Figure S29. Total charge produced, during CPE at 0.82 V (1.65 V vs NHE) for 7 h.

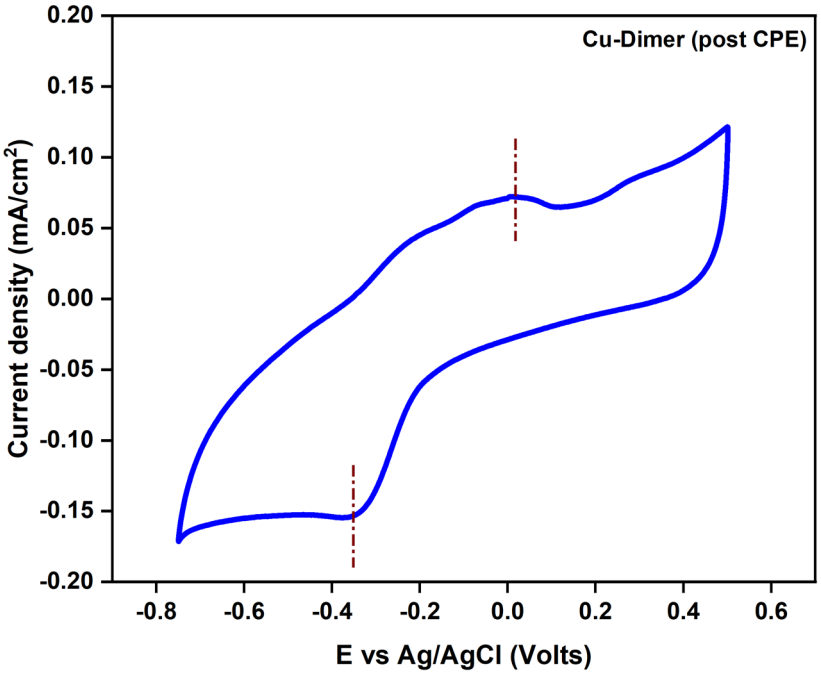

Figure S30. CV of FTO (with deposit) showing the redox events and shift in cathodic peak, after CPE at 0.82 V for 7 h.

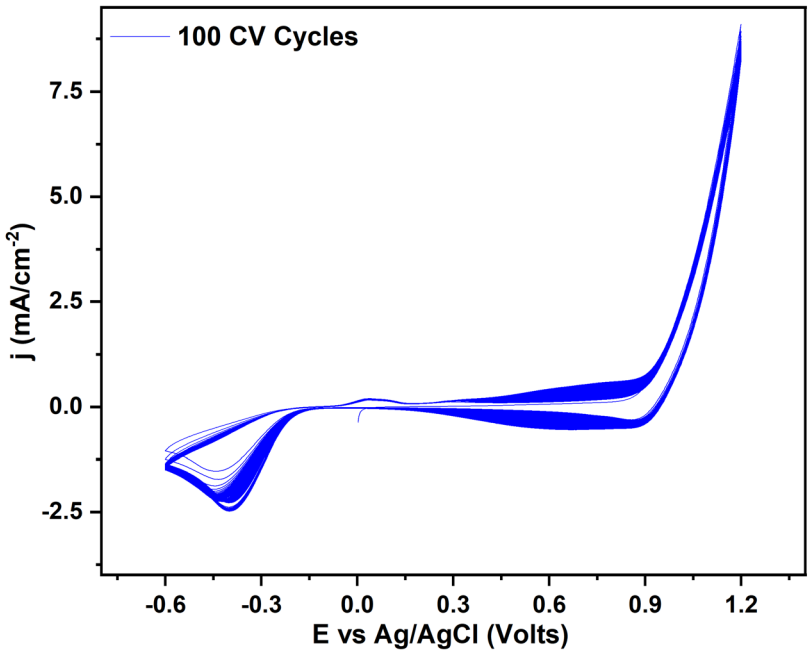

Figure S31. Consecutive 100 CV cycles of the deposited CuO material.

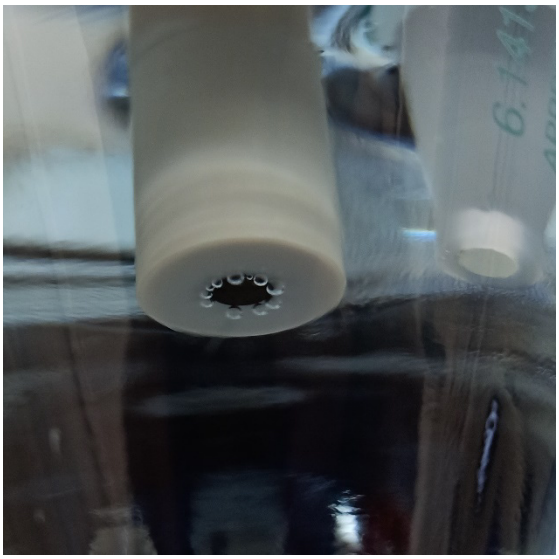

Figure S32. Evolution of O_2 bubbles during 100 CV cycles.

Characterization of the Cu deposit

SEM and EDX mapping

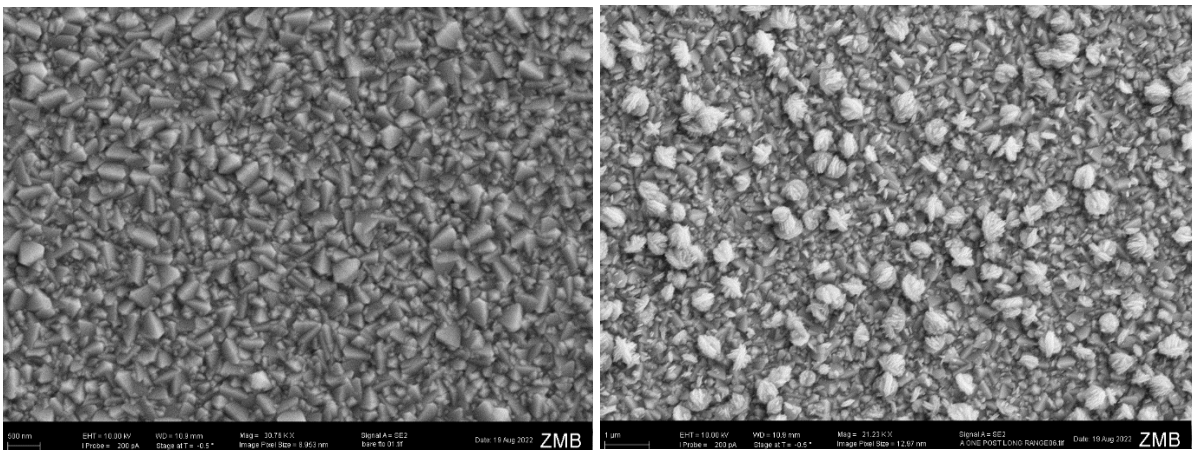

Figure S33. SEM images of FTO: (*left*) before bulk electrolysis and (*right*) after bulk electrolysis for 7 h.

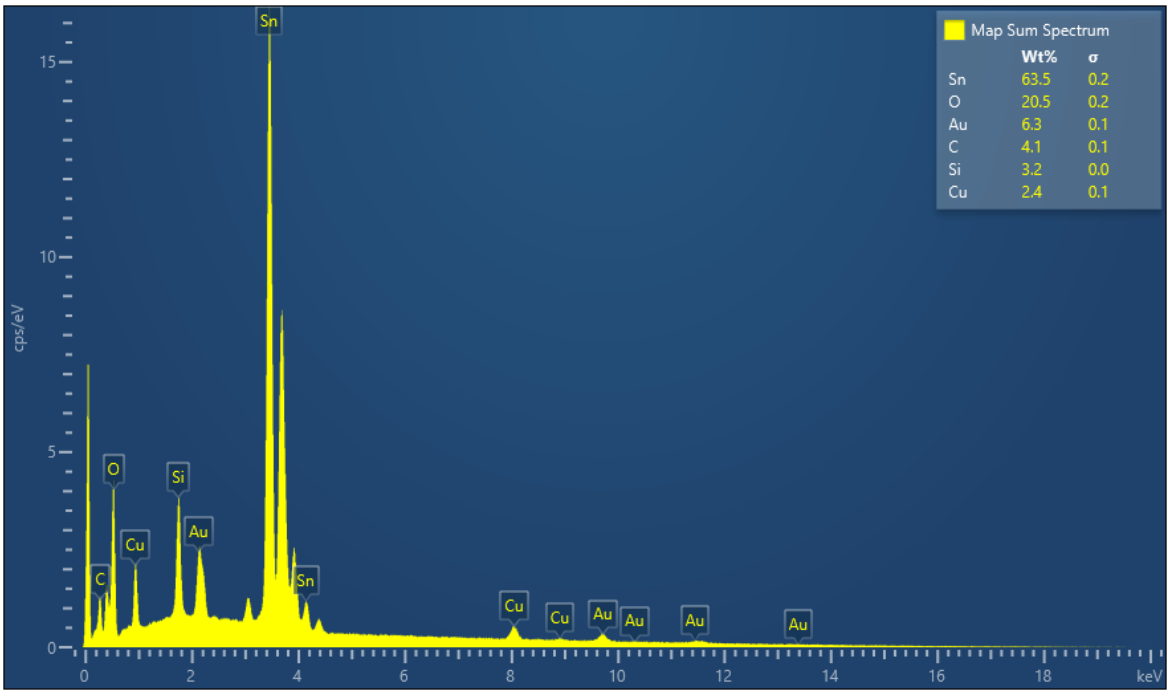

Figure S34. EDX quantification maps of FTO after bulk electrolysis for 7 h.

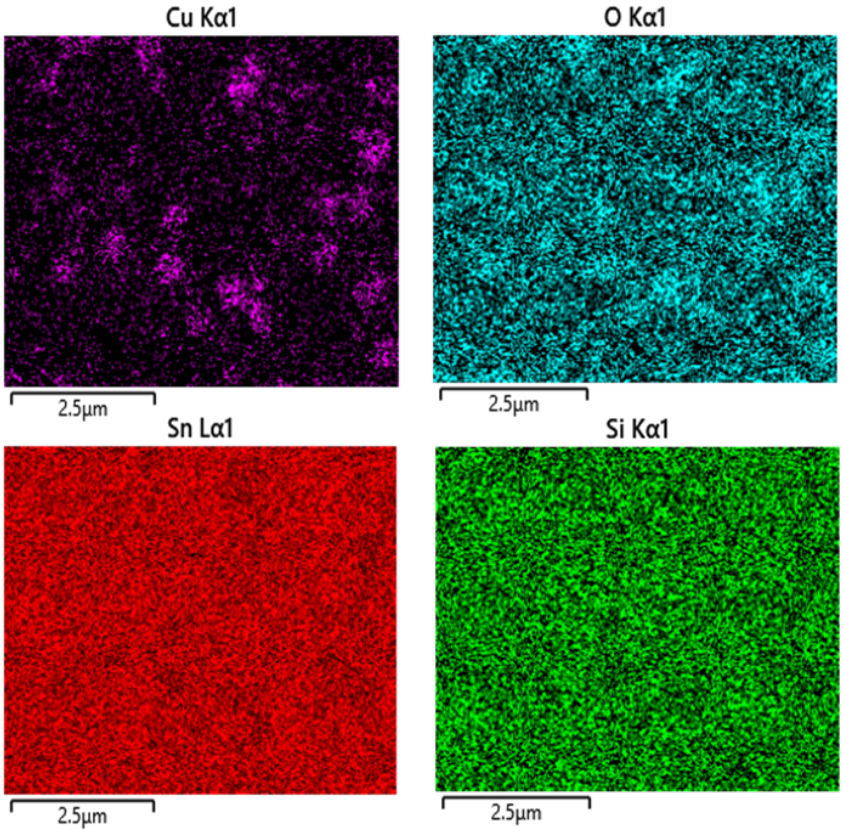

Figure S35. EDX elemental mapping of FTO after bulk electrolysis for 7 h.

X-ray photoelectron spectroscopy

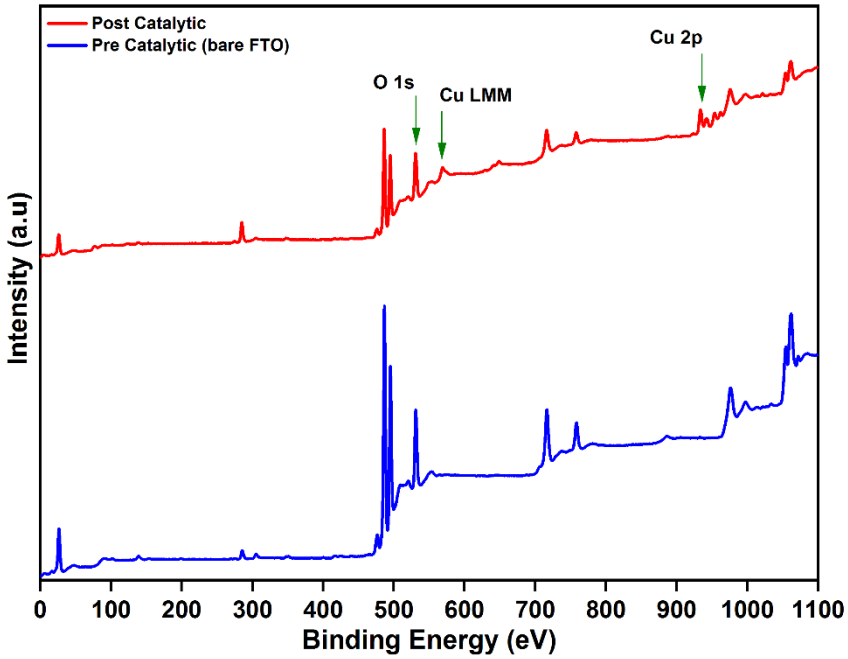

Figure S36. Survey XP spectrum of FTO before and after bulk electrolysis.

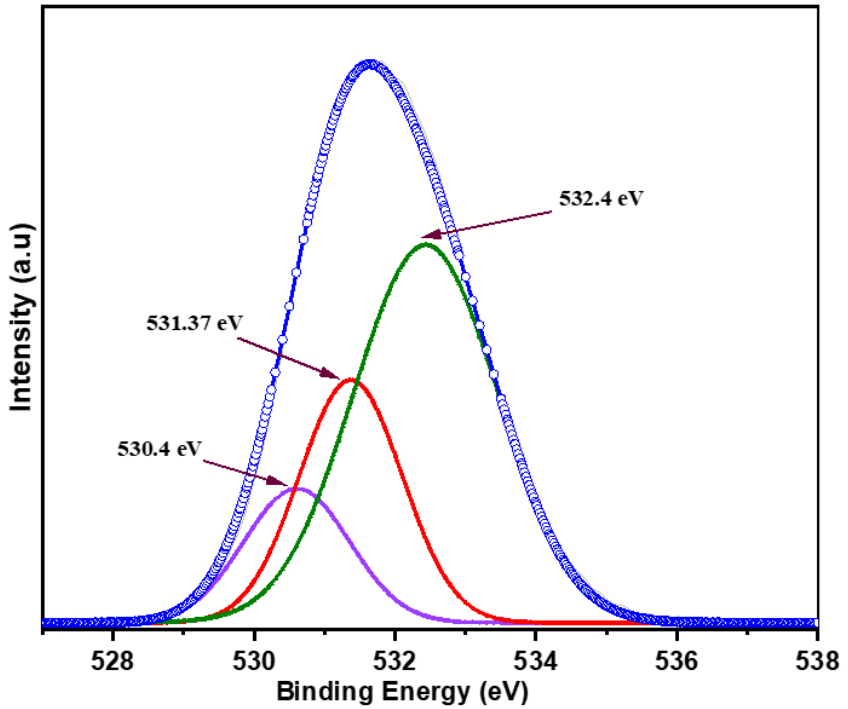

Figure S37. O1s XP spectrum of FTO after 7 h bulk electrolysis.

Raman spectroscopy

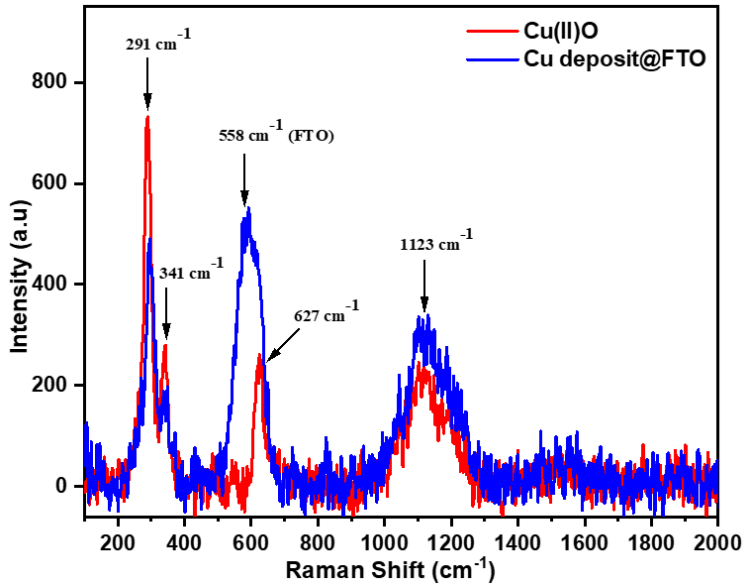

Figure S38. Overlay of Raman spectra of **CuO** and **Cu deposit** on FTO.

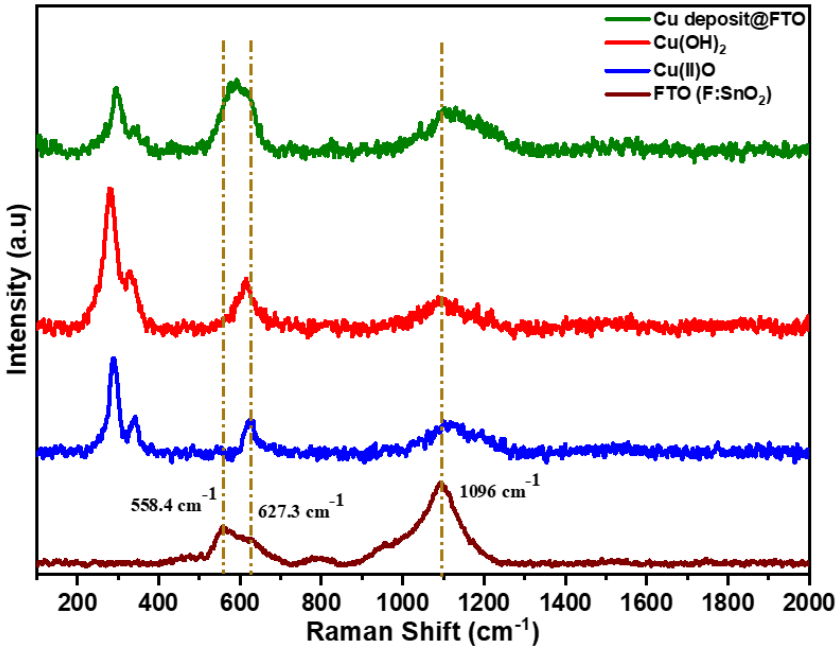

Figure S39. Raman spectra of **CuO, Cu(OH)$_2$**, **Cu deposit** and **bare FTO** depicting the overlap of FTO signals with **CuO** (*as observed in Cu deposit on FTO*).

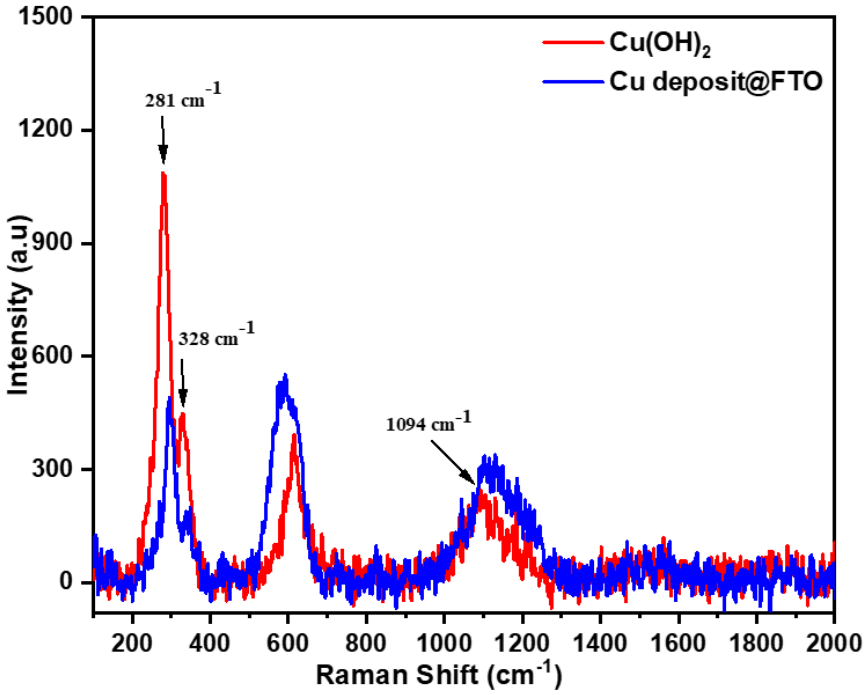

Figure S40. Overlay of Raman spectra of **$Cu(OH)_2$** and **Cu deposit on FTO** showing the shift in peaks.

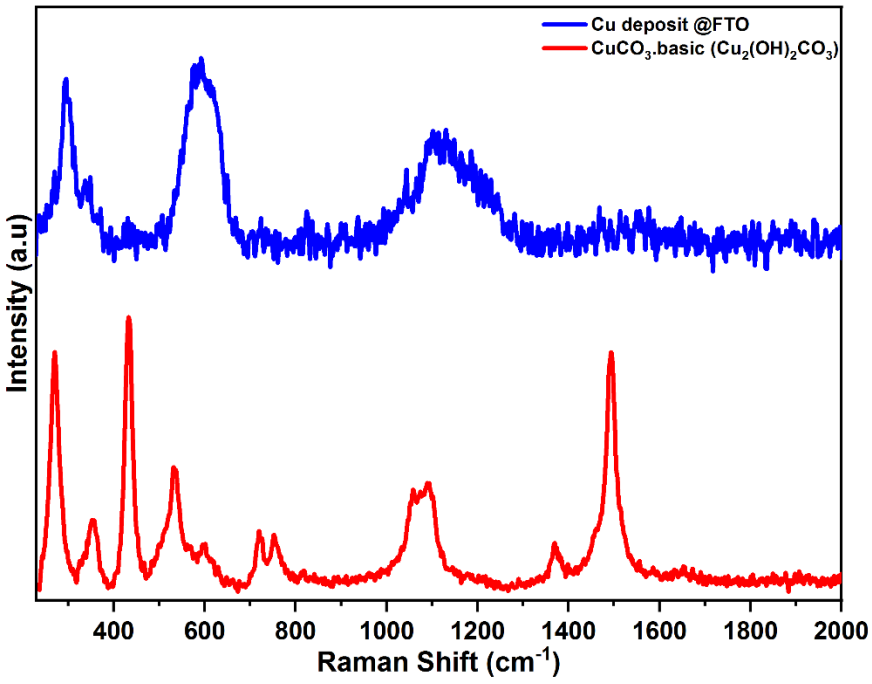

Figure S41. Raman spectra of **$CuCO_3$ basic** and **Cu deposit** on FTO.

FT-IR spectroscopy

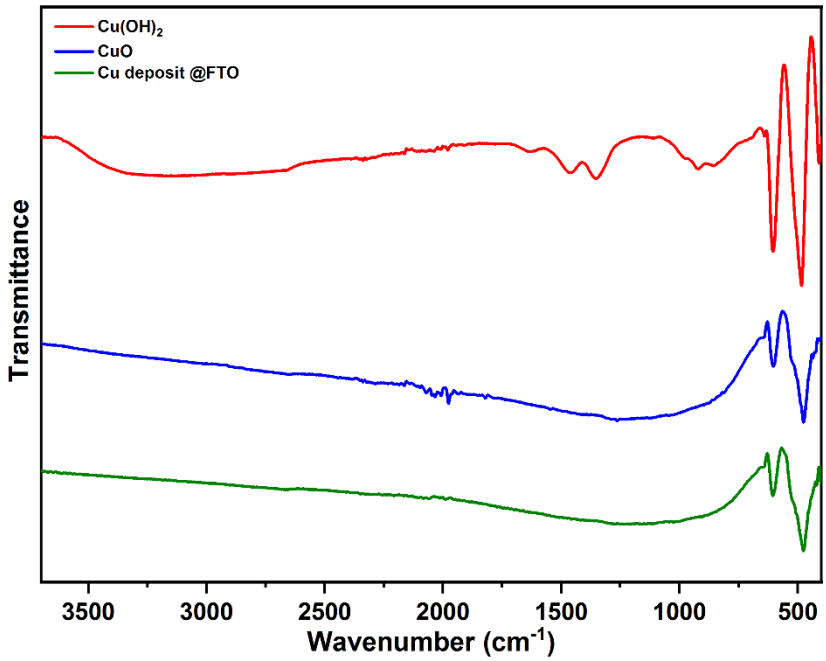

Figure S42. FT-IR spectrum of **Cu deposit** on FTO in comparison with CuO and $Cu(OH)_2$.

UV-Visible spectroscopy

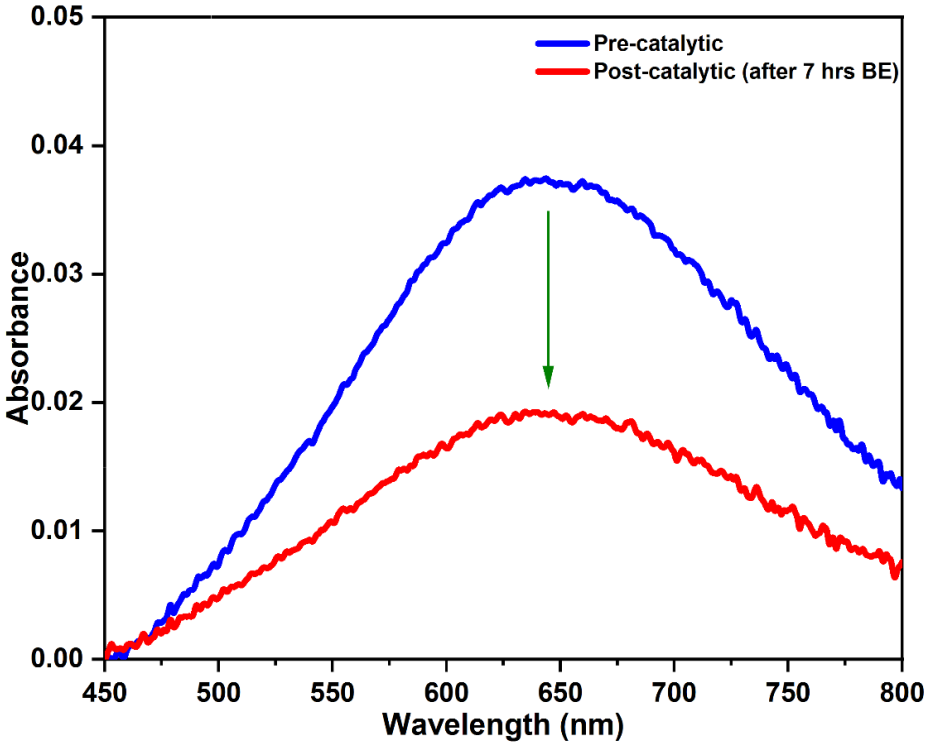

Figure S43. UV-Visible spectrum of **Cu-dimer** solution before (*pre-catalytic*) and after bulk electrolysis (*post-catalytic*).

Calculation of converted catalytic species (from pre & post UV-vis profiles, Fig. S43):

UV/vis: λ_{max} 655 nm (ε = 85 M^{-1} cm^{-1} , carbonate-bicarbonate buffer pH 10.5).

Concentration of Cu complex solution before bulk electrolysis = 0.5 mM

Concentration of Cu complex solution after 7 h bulk electrolysis = 0.19 mM

% of Cu complex conversion to CuO = 38 %

Table S7. Comparison of previously reported Cu-based heterogeneous electrocatalysts derived from molecular Cu complexes/Cu salts.

Cu complex	**Overpotential η (mV)**	**Buffer/pH**	**Ref.**
$CuSO_4$	740	Borate/7	[13]
Cu(cyclam)	700	Acetate/12	[14]
Cu(cyclam)	1051	Borate/9	[14]
$[Cu(TEOA)(H_2O)_2](SO_4)$	780	Acetate/12.4	[15]
$[Cu(TPA)\ H_2O](ClO_4)_2$	600	Borate/9.2	[16]
$Cu(en)_2$	540	Phosphate/12	[17]
$[Cu_4(pyalk)_4(OAc)_4](HNEt_3)(ClO_4)$	**960**	**Carbonate/10.5**	***This work***

Cyclam: 1,4,8,11-tetraazacyclotetradecane
TEOA: triethanolamine
TPA: tris(2-pyridylmethyl)amine)
en: ethylenediamine
pyalk: 2-(2'-pyridyl)-2-propanoate

References

1 C. F. Macrae, P. R. Edgington, P. McCabe, E. Pidcock, G. P. Shields, R. Taylor, M. Towler and J. Van De Streek, *J. Appl. Cryst,* 2006, **39**, 453–457.

2 O. V. Dolomanov, L. J. Bourhis, R. J. Gildea, J. A. K. Howard and H. Puschmann, *J. Appl. Cryst*, 2009, **42**, 339–341.

3 G. M. Sheldrick, *Acta Cryst. C*, 2015, **71**, 3–8.

4 G. M. Sheldrick, *Acta Cryst, A*, 2015, **71**, 3–8.

5 B. Ravel and M. Newville, *J. Synchrotron Rad.*, 2005, **12**, 537–541.

6 A. L. Ankudinov, B. Ravel, J. J. Rehr and S. D. Conradson, *Phys. Rev. B*, 1998, **58**, 7565.

7 T.-T. Li, S. Cao, C. Yang, Y. Chen, X.-J. Lv and W.-F. Fu, *Inorg. Chem*, 2015, **54**, 47.

8 H. Kuilya, N. Alam, D. Sarma, D. Choudhury and A. Kalita, *Chem. Commun.*, 2019, **55**, 5483–5486.

9 Q. Bai, X. Yang, S. Zheng, L. Hong, C. Dai, J. Lin, P. Wang and X. Liang, *Sustain. Energy Fuels*, 2022, **6**, 3643–3648.

10 F. Yu, F. Li, J. Hu, L. Bai, Y. Zhu and L. Sun, *Chem. Commun.*, 2016, **52**, 10377–10380.

11 J. Peisach and W. E. Blumberg, *Arch Biochem. Biophys.*, 1974, **165**, 691–708.

12 S. Stoll and A. Schweiger, *J. Magn. Reson.*, 2006, **178**, 42–55.

13 H.-H. Huang, J.-W. Wang, P. Sahoo, D.-C. Zhong and T.-B. Lu, *Chem. Commun.*, 2017, **53**, 22.

14 A. Prevedello, I. Bazzan, N. D. Carbonare, A. Giuliani, S. Bhardwaj, C. Africh, C. Cepek, R. Argazzi, M. Bonchio, S. Caramori, M. Robert and A. Artorel, *Chem. Asian J*. 2016, **11**, 1281-1287.

15 T. T. Li, S. Cao, C. Yang, Y. Chen, X. J. Lv and W. F. Fu, *Inorg. Chem.*, 2015, **54**, 3061–3067.

16 X. Liu, H. Jia, Z. Sun, H. Chen, P. Xu and P. Du, *Electrochem. Commun.*, 2014, **46**, 1–4.

17 X. Liu, S. Cui, M. Qian, Z. Sun and P. Du, *Chem. Commun.*, 2016, **52**, 5546–5549.